International Immunopharmacology 167 (2025) 115702

Contents lists available at ScienceDirect

International Immunopharmacology

journal homepage: www.elsevier.com/locate/intimp

Immune landscape and molecular regulators in renal interstitial fibrosis

Meng He, Ayijiaken Kasimumali, Shunian Guo, Hanyu Meng, Shu Rong *

Department of Nephrology, Shanghai General Hospital, Shanghai Jiao Tong University School of Medicine, Shanghai 200080, China.

ARTICLE INFO

Editor Name: Amorette Barber

Keywords:
Renal interstitial fibrosis
Immune mechanism
Hub genes

ABSTRACT

Renal interstitial fibrosis (RIF) represents the final pathological hallmark of chronic kidney disease (CKD) and is a pivotal factor leading to irreversible renal failure in end-stage renal disease (ESRD). It is highly clinically relevant and underpinned by complex immune mechanisms. This study aims to elucidate the molecular underpinnings of renal interstitial fibrosis, identify potential diagnostic biomarkers, and propose novel therapeutic targets. By integrating transcriptomic data from public Gene Expression Omnibus (GEO) datasets related to renal interstitial fibrosis, we uncovered a tight correlation between immune cell infiltration and key gene expression patterns. Differentially expressed genes (DEGs) identified from two datasets underwent Gene Ontology (GO) and Kyoto Encyclopedia of Genes and Genomes (KEGG) enrichment analyses, revealing significant involvement in immune responses, cell migration, and cytokine-mediated signaling pathways. Gene Set Enrichment Analysis (GSEA) further highlighted critical roles for chemokine signaling, immunoregulatory interactions, and interferon signaling in fibrotic progression. Construction of protein–protein interaction (PPI) networks using the STRING database and Cytoscape software led to the identification of several immune-related hub genes potentially central to fibrosis pathogenesis. These candidates were validated via merged dataset expression profiling and receiver operating characteristic (ROC) curve analysis. In addition, the significance of six hub genes (CD3D, CCL5, CXCL9, CCR5, IL7R, and CD2) in RIF was further validated through Quantitative Real-Time PCR and Western blot analyses in mouse models, as well as immunofluorescence staining in clinical patient samples. Finally, we performed regulatory network analysis involving microRNAs and transcription factors, revealing potential upstream modulators, and identified candidate therapeutic compounds through drug–gene interaction prediction and molecular docking. This study provides new insights into early diagnosis and immunotherapeutic strategies for renal interstitial fibrosis.

1. Introduction

RIF represents a pivotal pathological process underlying the progression of CKD, and is recognized as a final common pathway for nearly all forms of chronic renal injury [1]. Epidemiological data indicate a global CKD prevalence of approximately 10–15 % [2], with projections suggesting that CKD will become the second leading cause of death worldwide by 2030. As a hallmark of CKD progression, RIF has emerged as a critical indicator for monitoring disease severity and prognosis. In the United States, RIF and its sequelae—ESRD—have imposed a substantial public health burden. According to the National Kidney Foundation (NKF), nearly 14 % of the population suffers from CKD, with up to one-fifth progressing to ESRD [3], underscoring the high incidence and age-related risk escalation of RIF. In China, the prevalence of kidney diseases has risen steadily, driven by economic development and lifestyle transitions. The "Epidemiology of Chronic Kidney Disease in China" survey reported a CKD prevalence of 10.8 %, with approximately 40 % of affected individuals exhibiting varying degrees of RIF [4]. Given the accelerating pace of global population aging, the prevalence of RIF is expected to increase substantially, posing a mounting challenge to healthcare systems worldwide. RIF is influenced by an interplay of genetic susceptibility, environmental exposures, and behavioral factors. Key risk factors include longstanding hypertension, diabetes mellitus, chronic tubulointerstitial nephritis, obesity, and smoking. Notably, due to limitations in early diagnostic modalities, many patients are diagnosed only after the disease has reached an irreversible stage, thereby missing the optimal therapeutic window and leading to progressive renal dysfunction. Hence, identifying early molecular markers and elucidating the pathogenic mechanisms of RIF are crucial for halting CKD progression, improving patient prognosis, and enhancing quality of life.

RIF is characterized by irreversible structural and functional

* Corresponding author at: Department of Nephrology, Shanghai General Hospital, Shanghai Jiao Tong University School of Medicine, Shanghai 200080, China.
E-mail address: sophiars@126.com (S. Rong).

https://doi.org/10.1016/j.intimp.2025.115702
Received 15 June 2025; Received in revised form 8 October 2025; Accepted 12 October 2025
Available online 22 October 2025

alterations in the kidney resulting from chronic renal injury. Over time, normal renal parenchyma is replaced by excessive deposition of extracellular matrix (ECM), leading to progressive renal impairment and, ultimately, ESRD or renal failure [5]. Clinically, RIF manifests as proteinuria, tubular atrophy, tubular dilation, increased fibrogenesis, and ECM deposition—including collagen types I and III, and fibronectin [6]. Epithelial-to-mesenchymal transition (EMT) is a central event in RIF, wherein tubular epithelial cells acquire mesenchymal phenotypes and myofibroblastic functions [7]. This transformation promotes fibroblast proliferation, resulting in ECM overproduction and fibrotic remodeling [8]. Ultimately, renal replacement therapies such as dialysis or transplantation become the only viable options. Upon injury, resident fibroblasts and pericytes are activated, gaining contractile properties and producing inflammatory mediators and ECM proteins to initiate wound repair. However, in cases of recurrent or severe damage, ECM continues to accumulate, causing irreversible tissue injury, renal dysfunction, and potential organ failure [9]. The lack of effective early diagnostic markers and therapeutic targets remains a major obstacle in combating renal fibrosis, necessitating urgent investigation into the molecular mechanisms governing RIF pathogenesis [10].

Despite the availability of several treatment modalities aimed at mitigating CKD progression, current therapies primarily focus on slowing disease development rather than reversing established RIF. Conventional interventions such as blood pressure control, glycemic regulation, and immunosuppressive therapy attempt to suppress triggering factors to delay renal injury. However, these strategies demonstrate limited efficacy in patients with advanced fibrosis [11]. Therefore, identifying more specific therapeutic targets—particularly those involved in immune regulation, cytokine-mediated signaling pathways, and cell migration mechanisms—has become a central theme in renal fibrosis research.

The pathogenesis of RIF involves complex interplay among immune responses, inflammation, and ECM accumulation [12]. Immune cells—including T cells, B cells, dendritic cells, and macrophages—modulate local inflammatory responses and the renal immune microenvironment through direct cell–cell contact and the secretion of cytokines and chemokines [13], thereby influencing fibroblast activation, proliferation, and ECM deposition that collectively promote fibrotic progression [9]. T cells can either enhance or suppress fibrosis depending on their interaction with other immune cells and tubular epithelial cells. Macrophages play a crucial role in the immune response during renal fibrosis, with M1 macrophages producing pro-inflammatory cytokines and M2 macrophages releasing anti-inflammatory mediators, exhibiting dual roles throughout fibrotic development [14]. B cells contribute by producing antibodies and cytokines such as TGF-β and IL-6, and may modulate immune responses through interactions with T cells [15]. Dendritic cells serve as key antigen-presenting cells that activate T cells by processing antigens, including those derived from albumin via proteasome-dependent pathways in residual renal models, thus bridging innate and adaptive immunity [16]. Neutrophils exacerbate renal damage by releasing inflammatory mediators, reactive oxygen species, and proteases [17]. The immune microenvironment of renal fibrosis constitutes a dynamic and interwoven network where immune cells affect fibroblast behavior via cytokines, chemokines, and exosomes [18], fostering ECM accumulation and feedback loops that intensify renal injury. The persistent infiltration and activation of immune cells can exacerbate damage, triggering further fibroblast activation and ECM production, thereby creating a vicious cycle. As such, targeting immune cells and their signaling pathways presents a promising strategy for antifibrotic therapies. Delineating the regulatory mechanisms of immune cell involvement in fibrosis is thus of paramount importance for therapeutic development.

This study aims to elucidate the molecular underpinnings of renal interstitial fibrosis by integrating transcriptomics, immunological profiling, and bioinformatics analysis. Using both murine models and human clinical samples for experimental validation, we propose novel diagnostic and therapeutic strategies. Our investigation focuses on immune cell infiltration, differential gene expression, and immune-related gene function, providing a theoretical foundation for immunotherapeutic approaches in renal fibrosis. The analytical workflow is outlined in Fig. 1. The results of analyzing the data are shown in Figures 2-10.

2. Materials and methods

2.1. Dataset selection and preprocessing

To investigate gene expression alterations associated with RIF, we systematically searched the GEO database (https://www.ncbi.nlm.nih.gov/geo/) hosted by the National Center for Biotechnology Information (NCBI) using the keyword "Renal interstitial fibrosis." Based on inclusion criteria for relevance and sample size, two microarray datasets—GSE22459 and GSE76882—were selected for downstream analysis. Data were retrieved using the GEOquery R package (version 2.54.1). The GSE22459 dataset comprises tissue samples from 25 healthy controls and 40 patients with histologically confirmed RIF, while GSE76882 includes 99 control samples and 135 RIF samples. Detailed sample characteristics are summarized in Table 1. To ensure inter-sample comparability and mitigate batch effects, we applied quantile normalization using the limma package (version 3.54.2). Principal component analysis (PCA) was performed using R software (version 4.2.1) to assess sample distribution and identify potential outliers. Visualizations—including box plots and PCA plots—were generated using the ggplot2 package (version 3.4.4) to evaluate data quality and subgroup separation.

2.2. Differential gene expression analysis

To identify DEGs between RIF patients and healthy controls, we independently analyzed the GSE22459 and GSE76882 datasets using the limma package in *R. prior* to statistical analysis, duplicate entries were removed, and false discovery rate (FDR) correction was applied to adjust for multiple hypothesis testing. Genes with an absolute log2 fold change ($|\log2FC| \geq 1$ and adjusted p-value <0.05 were considered statistically significant. To visualize the DEGs, volcano plots and heatmaps were generated using the ggplot2 and ComplexHeatmap (version 2.13.1) packages, respectively. To identify commonly dysregulated genes across datasets, we integrated DEG lists from both GSE22459 and GSE76882 using the VennDiagram (version 1.7.3) and ggplot2 packages. Shared DEGs were then merged using the dplyr (version 1.0.9) and purrr (version 0.3.4) packages, resulting in a consolidated dataset comprising 124 control samples and 175 renal fibrosis samples. Volcano plots, heatmaps, and customized radar charts were constructed to illustrate the expression profiles and log2FC values of these DEGs using ggplot2 and ComplexHeatmap.

2.3. GO and KEGG pathway enrichment analysis

To explore the biological significance of the DEGs, GO enrichment analysis was performed using the clusterProfiler package (version 4.4.4) with the human genome as the reference background. The identified GO terms were categorized into three domains: biological processes (BP), cellular components (CC), and molecular functions (MF). Simultaneously, KEGG pathway analysis was conducted to identify signaling cascades potentially involved in renal interstitial fibrosis. The analysis employed stringent thresholds with a minimum gene count of 10, a maximum of 500, and statistical significance set at $p < 0.05$ and FDR $<$ 0.2. Gene ID conversion was performed using the org.Hs.eg.db package, and z-scores were calculated via the GOplot package (version 1.0.2). The results were visualized using network diagrams and bubble plots constructed with ggplot2, igraph (version 1.4.1), and ggraph (version 2.1.0), providing a comprehensive depiction of enriched functional

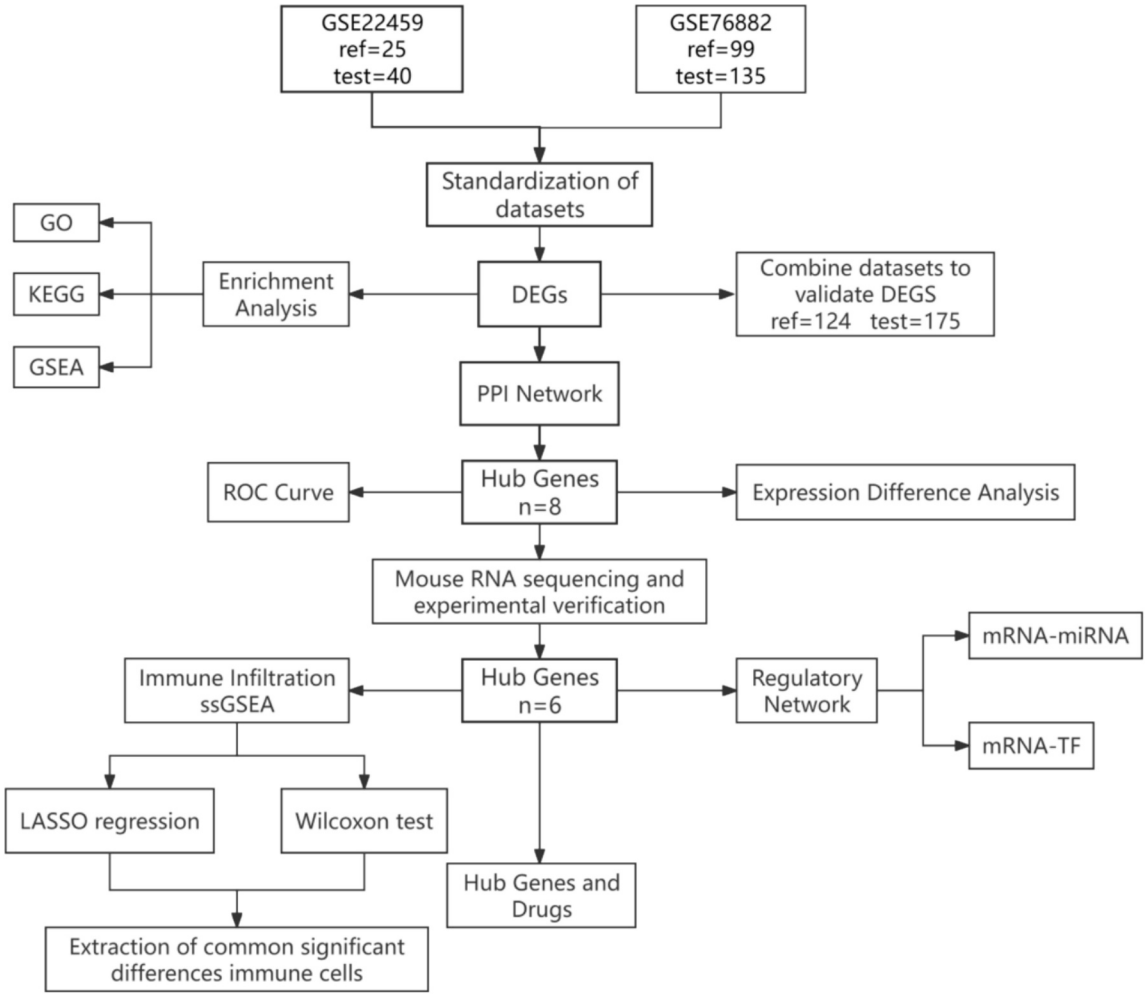

Fig. 1. Schematic workflow of the integrative analysis conducted in this study.

Table 1
Basic information of selected datasets.

GEO	Platform	Species	Tissues	IFTA (Test)	Non-IFTA (Ref)
GSE22459	GPL570	*Homo sapiens*	Kidney biopsy	40	25
GSE76882	GPL13158	*Homo sapiens*	Kidney biopsy	135	99

terms and pathways.

2.4. Gene set enrichment analysis (GSEA)

To investigate key biological signaling pathways and core regulatory genes, GSEA was performed using the clusterProfiler R package. The Molecular Signatures Database (MSigDB) Collections was used as the reference gene set, specifically the c2.cp.all.v2022.1.Hs.symbols.gmt for *Homo sapiens*. Enrichment significance was determined using the following criteria: normalized enrichment score ($|NES| > 1$, false discovery rate (FDR) < 0.25, and adjusted p-value < 0.05. These thresholds were used to identify significantly enriched pathways and core genes potentially involved in renal fibrosis. Visualization of the enrichment results was conducted using the ggplot2 package.

2.5. Protein–protein interaction (PPI) network construction and hub gene identification

To explore potential protein-level interactions among DEGs, we constructed a PPI network using the STRING database (https://string-db.org/). Co-expressed DEGs identified from the merged datasets were input into the STRING interface, and interaction data were subsequently exported into Cytoscape software (version 3.8.2) for advanced network visualization and analysis. To prioritize hub genes, we employed the CytoHubba plugin within Cytoscape and applied seven topological algorithms: Betweenness, Closeness, Degree, EPC, MNC, Radiality, and Stress. The top 10 genes ranked by each algorithm were selected, and genes overlapping across multiple methods were designated as key hub genes within the PPI network. Visualization of algorithmic intersections and gene importance was performed using ggplot2 through the construction of Upset plots and petal diagrams. Eight hub genes emerging from the consensus of all algorithms were ultimately selected for further study. These were re-imported into Cytoscape for final network visualization. To explore the correlation among clusters of these hub genes, Spearman correlation analyses were performed, and chord diagrams were generated using the circlize R package (version 0.4.1) to depict pairwise relationships among gene clusters.

2.6. Expression profiling and diagnostic evaluation of hub genes in renal fibrosis

To assess expression differences of the identified hub genes between

renal fibrosis and control groups, we performed statistical analysis in R. Normality was first assessed using Shapiro–Wilk tests, and variance homogeneity was tested via Chi-square tests. Depending on the distribution, Student's *t*-test was applied when assumptions were met, and Welch's t-test was used when heteroscedasticity was observed. Boxplots, dot plots, and violin plots were generated with the ggplot2 package to visualize gene expression patterns, with statistical significance annotated as follows: ns for $p \geq 0.05$, * for $p < 0.05$, ** for $p < 0.01$, and *** for $p < 0.001$. To evaluate the diagnostic potential of hub genes, receiver operating characteristic (ROC) curve analysis was conducted using the pROC package (version 1.18.0). The area under the ROC curve (AUC) was calculated to assess the sensitivity and specificity of each gene. Genes with AUC values greater than 0.75 were considered to possess promising diagnostic utility for renal interstitial fibrosis. Final ROC visualizations were rendered using ggplot2.

2.7. Construction of mRNA–miRNA regulatory networks and key miRNA Prediction

To predict the microRNAs (miRNAs) that potentially target the identified hub genes, we integrated data from four publicly available databases: TargetScan (v8.0), StarBase (v3.0), miRTarBase (v8.0), and miRDB (v6.0). miRNAs that were predicted by at least two of these databases were selected for further analysis. Based on validated or predicted interactions between these miRNAs and their corresponding mRNA targets, a co-expression network was constructed and visualized using Cytoscape software. In parallel, transcription factors (TFs) known to regulate hub genes at the transcriptional level were identified through ChIPBase (http://rna.sysu.edu.cn/chipbase/). TFs were considered relevant if the sum of supporting evidence from upstream and downstream regulatory interactions exceeded 10. These TF–mRNA interactions were visualized to construct the transcriptional regulatory network using Cytoscape, thereby delineating the multilayered control of hub gene expression in renal fibrosis.

2.8. Immune cell infiltration analysis

To quantify the relative abundance of immune cell infiltration across samples, we applied the single-sample gene set enrichment analysis (ssGSEA) algorithm implemented in the R package GSVA [19]. A reference gene set consisting of 24 immune cell-type markers was used, as defined by Bindea et al.(2013) in Immunity [20]. The resulting enrichment scores provided an immune cell infiltration matrix for the combined dataset. We visualized differences in immune cell infiltration between control and renal fibrosis groups using ggplot2, and performed statistical comparisons to identify immune subsets with significant variation. Spearman correlation coefficients were then calculated among all immune cell types to evaluate intercellular relationships, and the results were rendered as heatmaps (via ComplexHeatmap, v2.13.1) and scatter plots using ggplot2. Furthermore, Least Absolute Shrinkage and Selection Operator (LASSO) regression, implemented via the glmnet R package, was employed to select the most representative immune cell types capable of distinguishing between renal fibrosis and normal samples. Lastly, we assessed the correlation between each hub gene and immune cell subtype using Spearman's method, and generated corresponding scatter plots to illustrate these associations.

2.9. Drug prediction and molecular docking analysis

To identify potential therapeutic agents targeting the hub genes, we initially performed literature-based drug–gene association mining using the Coremine Medical platform (https://coremine.com/medical). Candidate small molecules and natural compounds potentially interacting with the six core hub genes were selected based on frequency and relevance. These candidates were used to build a drug–gene interaction network, which was subsequently visualized in Cytoscape (v3.9.1) to depict multi-target interaction patterns. Next, the 3D molecular structures of selected compounds were retrieved from the PubChem database in SDF format and uploaded to the SwissTargetPrediction platform (https://www.swisstargetprediction.ch/) for computational target prediction. Only targets with a non-zero prediction probability were retained for further docking analysis. To ensure docking accuracy, the predicted protein targets were preprocessed using PyMol software by removing water molecules and pre-existing ligands. AutoDock software was then used to perform molecular docking simulations, which involved hydrogenation, charge calculation, grid box definition, and ligand–receptor docking. The binding free energy (ΔG) was used as a key criterion to evaluate docking affinity: a binding energy <0 kcal/mol indicated spontaneous interaction, and values < -5 kcal/mol signified strong binding potential. To provide intuitive insight into ligand–receptor binding conformations, we employed PyMol 2.3.0 for three-dimensional structural visualization and LigPlot+ v2.2 for two-dimensional schematic representations. These visualizations highlighted key interaction forces—such as hydrogen bonding and hydrophobic interactions—thereby facilitating rational drug design and target validation.

2.10. Animal studies

All animal procedures in this study were approved by the Institutional Animal Care and Use Committee (IACUC) of Shanghai General Hospital (Approval No. 2025AWS038) and conducted in accordance with the Guide for the Care and Use of Laboratory Animals published by the U.S. National Institutes of Health. Male wild-type (WT) C57BL/6 J mice (6–8 weeks old, weighing 22–25 g) were purchased from the Experimental Animal Center of Shanghai General Hospital. Mice were housed under specific-pathogen-free (SPF) conditions with a 12-h light/dark cycle (lights on at 07:00) at a constant temperature of 24 °C. They were maintained five per cage with ad libitum access to sterilized food (Ke'ao Xieli Feed Co., Beijing, China) and water. Cages, bedding (corncob), and water were autoclaved, and bedding was changed three times weekly. All animals were monitored daily by veterinary staff and exhibited no signs of pain or pathology requiring intervention. Mice were randomly assigned to two groups ($n = 7$ per group): sham-operated controls and a unilateral ureteral obstruction (UUO) model group. For UUO surgery, mice were anesthetized via intraperitoneal injection of pentobarbital sodium (8 mg/kg). A left flank incision was made to expose the left kidney and ureter, followed by double ligation of the ureter using 4–0 nylon sutures. Sham-operated mice underwent the same surgical exposure without ureteral ligation. All surgical procedures and subsequent analyses were performed under blinded conditions. Two weeks post-surgery, mice were euthanized, and both kidneys were harvested for Quantitative Real-Time PCR, histological evaluation, and Western blotting.

2.11. RNA extraction and quantitative real-time PCR (qRT-PCR)

Approximately 20 mg of kidney tissue was homogenized in 1 mL TRIzol reagent (Invitrogen, USA) with two 3 mm steel beads using a tissue homogenizer at 65 Hz for 60 s on ice. Samples were lysed on ice for an additional 5 min and then transferred to new RNase-free tubes. Following the addition of 200 μL chloroform, tubes were vortexed and allowed to stand for 3 min. Samples were centrifuged at 12,000 rpm for 15 min at 4 °C, and the upper aqueous phase was carefully collected and transferred to fresh tubes. An equal volume (0.5 mL) of isopropanol was added, mixed thoroughly, and incubated at −20 °C for 30 min or overnight. After a second centrifugation (12,000 rpm, 15 min, 4 °C), the supernatant was discarded. The RNA pellet was washed with 1 mL of 70 % ethanol (prepared with DEPC-treated water), vortexed, and centrifuged again under the same conditions. Residual ethanol was removed, and the pellet was air-dried in a biosafety cabinet for 5–10 min. Finally, RNA was dissolved in 30 μL DEPC-treated water, and either stored at

−80 °C or used immediately for reverse transcription. For cDNA synthesis, 1 μg of total RNA was subjected to genomic DNA removal and reverse transcription using a commercial kit. The 20 μL reaction system included gDNA eraser, 2× reverse transcription buffer, and diluted RNA template. The reaction was conducted at 50 °C for 15 min and terminated at 75 °C for 5 min, with cDNA stored at 4 °C until use. Quantitative real-time PCR was performed using a SYBR Green qPCR Master Mix (Takara, Japan) in a 15 μL system comprising 3 μL diluted cDNA, 0.3 μL each of forward and reverse primers (10 μmol/L), and 7.5 μL 2× SYBR mix, supplemented with nuclease-free water. All reactions were run in duplicate using GAPDH as the internal control. Amplification was carried out on a real-time PCR system under the following cycling conditions: 95 °C for 1 min (initial denaturation), followed by 40 cycles of 95 °C for 10 s and 60 °C for 30 s. A melt curve analysis was conducted at 95 °C for 15 s, 60 °C for 60 s, and 95 °C for 15 s to confirm specificity. Relative gene expression levels were calculated using the 2ˆ−ΔΔCt method. All primers used in this study, including those for the target genes and the housekeeping gene GAPDH, are listed in Table 2. GAPDH expression served as the internal reference to normalize RNA quantity and quality across samples.

2.12. Western blot analysis

Renal tissue from mice was lysed in RIPA buffer supplemented with 1× protease inhibitor cocktail and 1× phosphatase inhibitor. The homogenates were incubated on ice for at least 10 min, then mechanically homogenized to ensure complete tissue disruption. Lysates were centrifuged at 12,000 ×*g* for 15 min at 4 °C, and the supernatants were carefully collected. Protein concentration was determined using a bicinchoninic acid (BCA) assay. Equal amounts of protein were separated by 8 % SDS–PAGE and transferred onto polyvinylidene fluoride (PVDF) membranes. After blocking, membranes were incubated with primary and corresponding HRP-conjugated secondary antibodies. Bands were visualized using an automated chemiluminescence imaging system, and densitometric quantification was performed using ImageJ software by comparing the target band intensity relative to the internal control (GAPDH). The list of primary and secondary antibodies used is provided in Table 3.

2.13. Human renal biopsy samples

Renal biopsy is a routine component of clinical diagnosis, with samples sourced from the Department of Pathology at Shanghai General Hospital. Renal biopsy samples were collected from patients diagnosed with CKD who had not yet initiated dialysis treatment at the time of biopsy. Control samples were obtained from CKD Stage 1 patients confirmed by renal biopsy, while fibrotic samples were derived from CKD Stage 5 patients confirmed by biopsy. All studies were conducted in accordance with the ethical principles outlined in the Declaration of Helsinki and were approved by the Research Ethics Committee of Shanghai General Hospital, with informed consent obtained from all participants(Yuanlun Kuai [2025] No. 226).

Table 3
Primary and secondary antibodies used in Western blotting.

Antibody	Host	MW (kDa)	Company	Catalog No.
Fibronectin(FN)	Rabbit	256 kDa	Abcam	ab45688
phospho-smad3(S423/S425)	Rabbit	56 kDa	HuaAn Biotech	ET1609–41
α-Smooth Muscle Actin(a-SMA)	Rabbit	40kd	HuaAn Biotech	ET1607–53
CD3D	Rabbit	17 kDa	Affinity	DF6370
CCL5	Rabbit	15kd	HuaAn Biotech	ET1705–70
GAPDH	Mouse	38kd	Proteintech	60,004–1-lg
Goat anti Rabbit IgG-HRP	Rabbit	–	Genexpan	GXP438200
Goat anti Mouse IgG-HRP	Mouse	–	Genexpan	GXP341397

2.14. Immunofluorescence

Kidney tissue samples were paraffin-embedded and sectioned into 4–5 μm thick slices using a microtome. Sections were mounted onto glass slides and pre-dried in a 60 °C oven for 1 h to ensure firm adhesion. Paraffin removal was performed by immersing slides in xylene twice for 10 min each. Rehydration was achieved by sequential incubation in 100 %, 95 %, 85 %, and 75 % ethanol for 5 min each, followed by rinsing in distilled water. For antigen retrieval, sections were placed in 0.01 M citrate buffer (pH 6.0) or EDTA buffer (pH 8.0), heated to boiling using a microwave, and maintained at 80 °C for 20 min. After cooling to room temperature, nonspecific binding was blocked with 5 % bovine serum albumin (BSA) or 5 % goat serum at room temperature for 1 h. Slides were then washed three times with PBS, each wash lasting 5 min. Sections were incubated overnight at 4 °C with appropriately diluted primary antibodies, selected according to experimental requirements and optimized based on supplier recommendations. The next day, slides were washed three times with PBS, followed by incubation with fluorophore-conjugated secondary antibodies for 1 h at room temperature. Secondary antibodies were species-specific, matching the source of the primary antibodies. After another series of PBS washes (3 × 5 min), nuclei were counterstained with DAPI (4′,6-diamidino-2-phenylindole) for 5–10 min at room temperature, then rinsed with PBS. Slides were mounted using antifade mounting medium and covered with a coverslip without introducing air bubbles. Fluorescent signals were examined and documented using a fluorescence microscope, assessing signal intensity, distribution, and localization based on the experimental design.

2.15. Masson's trichrome staining of kidney tissue sections

Kidney samples were fixed in 10 % neutral-buffered formalin for 48 h, followed by dehydration, paraffin embedding, and sectioning at 4 μm thickness. Paraffin was removed by sequential immersion in xylene, absolute ethanol, and 75 % ethanol, followed by rinsing in tap water and distilled water. Sections were stained with hematoxylin-iron chloride solution for 10 min and washed with distilled water. Differentiation was performed using acidic ethanol for 5–15 s. *Re*-blueing was carried out using Masson's blueing reagent for 3–5 min. Cytoplasm was stained with Ponceau-Fuchsin for 3–5 min, followed by washing with a weak acid

Table 2
Primer sequences used for quantitative real-time PCR.

Gene	Forward primer(5′-3′)	Reverse primer(3′-5′)
CCL5(mouse)	GCTGCTTTGCCTACCTCTCC	TCGAGTGACAAACACGACTGC
CD3D(mouse)	CTTGGGCAAAGGCGTTCTG	CAGTTCTGGCACATTCGGTAAT
CCR5(mouse)	ATGGATTTTCAAGGGTCAGTTCC	CTGAGCCGCAATTTGTTTCAC
IL7R(mouse)	GCGGACGATCACTCCTTCTG	GCATTTCACTCGTAAAAGAGCCC
CD2(mouse)	GATGAGAAACGACAGTGGCACC	CCAGTGGATCATGGGCTTTGAG
CXCL9(mouse)	GGAGTTCGAGGAACCCTAGTG	GGGATTTGTAGTGGATCGTGC
GAPDH(mouse)	CATCACTGCCACCCAGAAGACTG	ATGCCAGTGAGCTTCCCGTTCAG

working solution for 1 min. Phosphomolybdic acid was used for differentiation (2 min), followed by another 1-min rinse. Collagen fibers were then stained with aniline blue for 1–2 min and washed again with the weak acid solution. After staining, sections were dehydrated through a graded ethanol series, cleared in xylene, and mounted using neutral balsam. Care was taken to avoid air bubbles. The slides were then air-dried and observed under a light microscope.

2.16. Statistical analysis

Data are presented as mean ± SEM. Statistical analyses were conducted using GraphPad Prism version 8.0 (GraphPad Software, San Diego, CA, USA). Normality was assessed using the Kolmogorov–Smirnov test. For comparisons between two groups, a two-tailed Student's *t*-test was used for normally distributed data, while the Mann–Whitney *U* test was employed for nonparametric data. One-way ANOVA followed by Tukey's post hoc test was used for comparisons among multiple groups with a single variable. For comparisons involving three or more non-normally distributed groups, the Kruskal–Wallis test was used. For multi-variable, multi-group comparisons, two-way ANOVA followed by Tukey's post hoc test was performed. Pearson correlation analysis was used where appropriate. A p value <0.05 was considered statistically significant.

3. Results

3.1. Data normalization and differential gene expression analysis

To investigate gene expression patterns and identify DEGs, we performed normalization on the GSE22459 and GSE76882 datasets. Boxplots in Fig. 2A and Fig. 2C display the distribution of expression values across all samples in each dataset. The data show uniform expression levels without significant deviations, indicating successful normalization. PCA plots in Fig. 2B and Fig. 2D demonstrate the clustering of samples along the first two principal components. These plots reveal clear segregation among sample groups, highlighting distinct transcriptional profiles and supporting the suitability of the datasets for further differential expression analysis. DEGs were identified using the limma package in R, with a threshold of adjusted $p < 0.05$ and $|\log_2 \text{fold change}| \geq 1$. Volcano plots in Fig. 2E and Fig. 2G visualize the distribution of significantly upregulated and downregulated genes in the GSE22459 and GSE76882 datasets, respectively. These plots highlight robust transcriptional alterations, providing a foundation for gene prioritization in subsequent analyses. Heatmaps in Fig. 2F and Fig. 2H display the expression patterns of DEGs across all samples, including 92 upregulated and 8 downregulated genes in GSE22459, and 294 upregulated and 164 downregulated genes in GSE76882. These heatmaps clearly depict expression variation and assist in pinpointing candidate genes potentially involved in renal interstitial fibrosis. To identify overlapping DEGs, a Venn diagram in Fig. 2I shows 47 genes commonly differentially expressed in both datasets. A combined volcano plot in Fig. 2J confirms the consistency of these 47 shared DEGs across datasets, reinforcing their relevance. Further characterization of these shared DEGs is shown in Fig. 2K and Fig. 2L, which present a radar plot and a heatmap, respectively. These visualizations provide an integrated view of gene expression patterns, underscoring the distinct expression profiles of these genes in the merged dataset. Through comprehensive DEG analysis, we identified multiple genes that may play pivotal roles in the progression of renal interstitial fibrosis. These genes represent promising candidates for early diagnosis and potential targets for therapeutic intervention.

3.2. GO and KEGG enrichment analysis of common DEGs

To gain deeper insights into the potential biological functions of the 47 commonly DEGs in renal interstitial fibrosis, we performed GO and KEGG pathway enrichment analyses. Fig. 3A presents bar plots illustrating GO and KEGG enrichment results across three GO categories: BP, CC, and MF. The x-axis denotes significantly enriched terms. The results reveal that the shared DEGs are primarily enriched in immune-related biological processes, including lymphocyte differentiation, leukocyte migration, monocyte differentiation, and T cell differentiation. Moreover, strong enrichment was observed in key signaling pathways such as the chemokine signaling pathway. Fig. 3B—D display network diagrams for enriched BP, CC, and MF terms, respectively. In these diagrams, orange nodes represent GO terms and green nodes represent associated genes, with edges indicating their interactions. The network structure provides an intuitive overview of the functional relationships among terms. For example, lymphocyte differentiation is tightly linked to immune cell function, while chemokine activity and chemokine receptor binding are directly involved in the regulation of immune cell migration. In the BP category, the DEGs are significantly enriched in pathways associated with immune response regulation, such as lymphocyte differentiation, leukocyte migration, monocyte differentiation, and T cell development—all processes critical to immune function and cellular modulation. Enrichment in the CC category highlights components such as the external side of the plasma membrane, secretory granule lumen, cytoplasmic vesicle lumen, and vesicle lumen, suggesting these cellular structures may play roles in the progression of renal interstitial fibrosis. In terms of MF, enriched terms include chemokine activity, chemokine receptor binding, serine-type endopeptidase activity, and serine-type peptidase activity, which are essential for immune cell migration, inflammatory signaling, and tissue remodeling. Fig. 3E and 3F present KEGG pathway enrichment networks. These visualizations emphasize the involvement of DEGs in several immune-related pathways, including the chemokine signaling pathway, cytokine–cytokine receptor interaction, and hematopoietic cell lineage. These pathways are known to be critical in immune responses, inflammation, and immune evasion, reinforcing the biological relevance of the DEGs in the context of renal interstitial fibrosis. Together, the GO and KEGG enrichment analyses highlight the significant roles of the 47 shared DEGs in immune regulation, cell migration, and signal transduction. These findings offer new perspectives for understanding the molecular mechanisms of renal interstitial fibrosis and point to potential therapeutic targets.

3.3. GSEA analysis reveals significant enrichment in immune response, cell migration, and renal function pathways

Building upon the GO and KEGG enrichment analyses that identified key immune-related biological processes and signaling pathways involved in renal interstitial fibrosis, we further applied GSEA to the combined dataset. This approach enabled a more systematic investigation of coordinated gene expression programs and signaling modules implicated in fibrosis-associated immune mechanisms. Fig. 4A and 4B display the results of the GSEA conducted on the integrated dataset. Fig. 4A presents a bubble plot of the top ten significantly enriched biological processes and pathways. Bubble size indicates the number of genes contributing to each term, while bubble color reflects the normalized enrichment score (NES), with warmer colors (e.g., red) denoting stronger enrichment. The analysis revealed that the most significantly enriched gene sets were primarily associated with immune responses, cell migration, and fibrotic activity. Notably, pathways such as chemokine signaling, immunoregulatory interactions, and interferon signaling were highly enriched, underscoring the central role of the immune system in renal interstitial fibrosis. Additionally, terms related to proximal tubule transport and cytokine signaling were also strongly enriched, suggesting their potential involvement in the onset and progression of fibrotic remodeling. Fig. 4B presents enrichment ridge plots (mountain plots), which offer an intuitive view of how biological processes are distributed across the ranked gene list. These plots illustrate the enrichment patterns for various immune-related and inflammatory pathways, including immunoregulation and cytokine-mediated

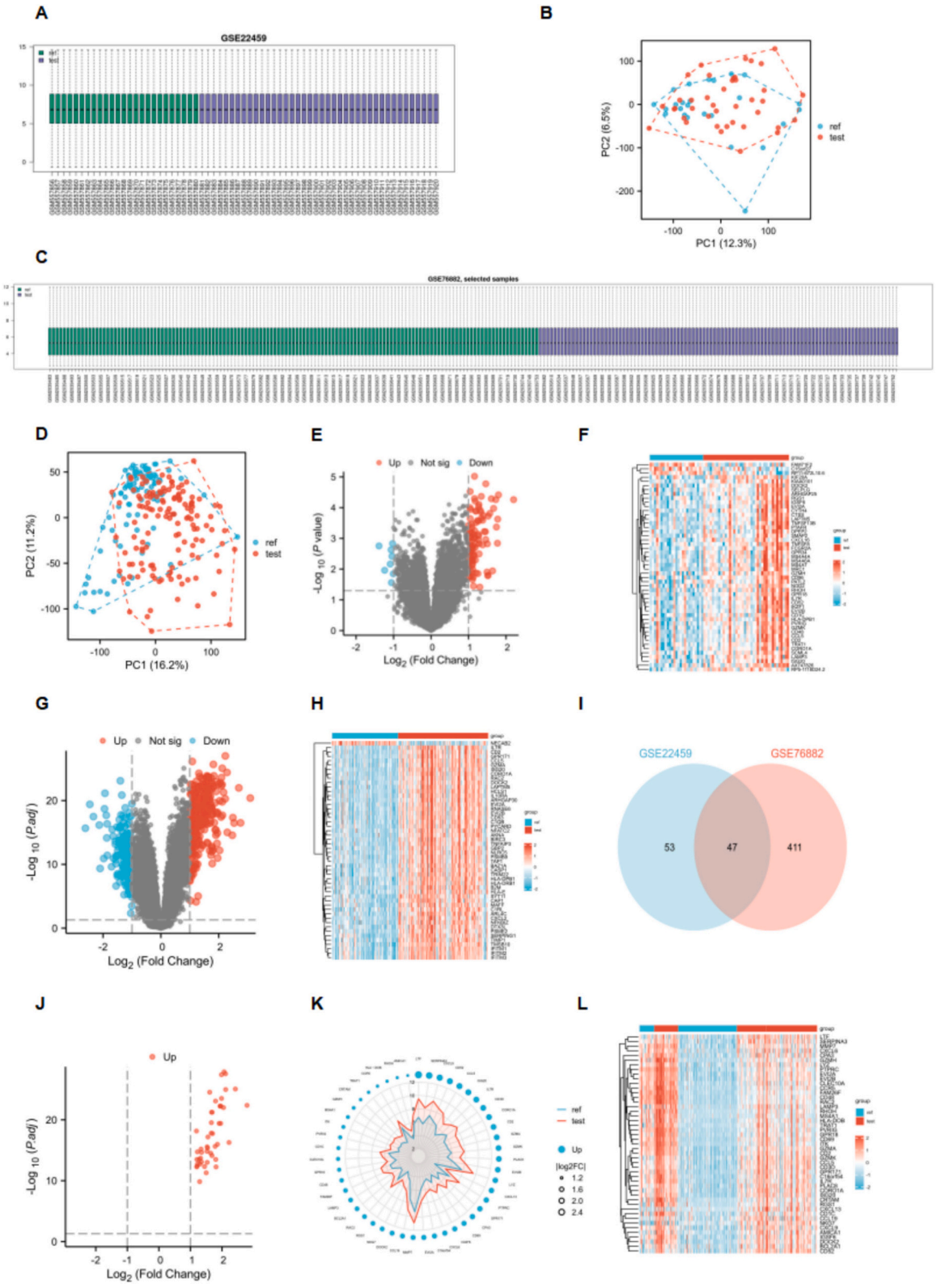

Fig. 2. Distribution characteristics after dataset normalization and identification of DEGs. (A) Boxplot of gene expression values across all samples in the GSE22459 dataset. (B) PCA plot showing the distribution of sample expression values in GSE22459. (C) Boxplot of gene expression values across all samples in the GSE76882 dataset. (D) PCA plot showing the distribution of sample expression values in GSE76882. (E) Volcano plot of DEGs in GSE22459 identified using the limma package in R. Genes with adjusted *p*-value <0.05 and $|\log_2 FC| \geq 1$ were considered significantly differentially expressed. (F) Heatmap of DEGs in GSE22459, including 92 upregulated and 8 downregulated genes. (G) Volcano plot of DEGs in GSE76882 identified using the limma package in R with the same significance thresholds. (H) Heatmap of DEGs in GSE76882, including 294 upregulated and 164 downregulated genes. (I) Venn diagram showing 47 overlapping DEGs shared between GSE22459 and GSE76882 datasets. (J) Volcano plot of the merged expression levels of the 47 shared DEGs across both datasets. (K) Radar chart illustrating the expression characteristics of the 47 shared DEGs in the integrated dataset. (L) Heatmap of the 47 shared DEGs in the combined dataset, highlighting their differential expression patterns.

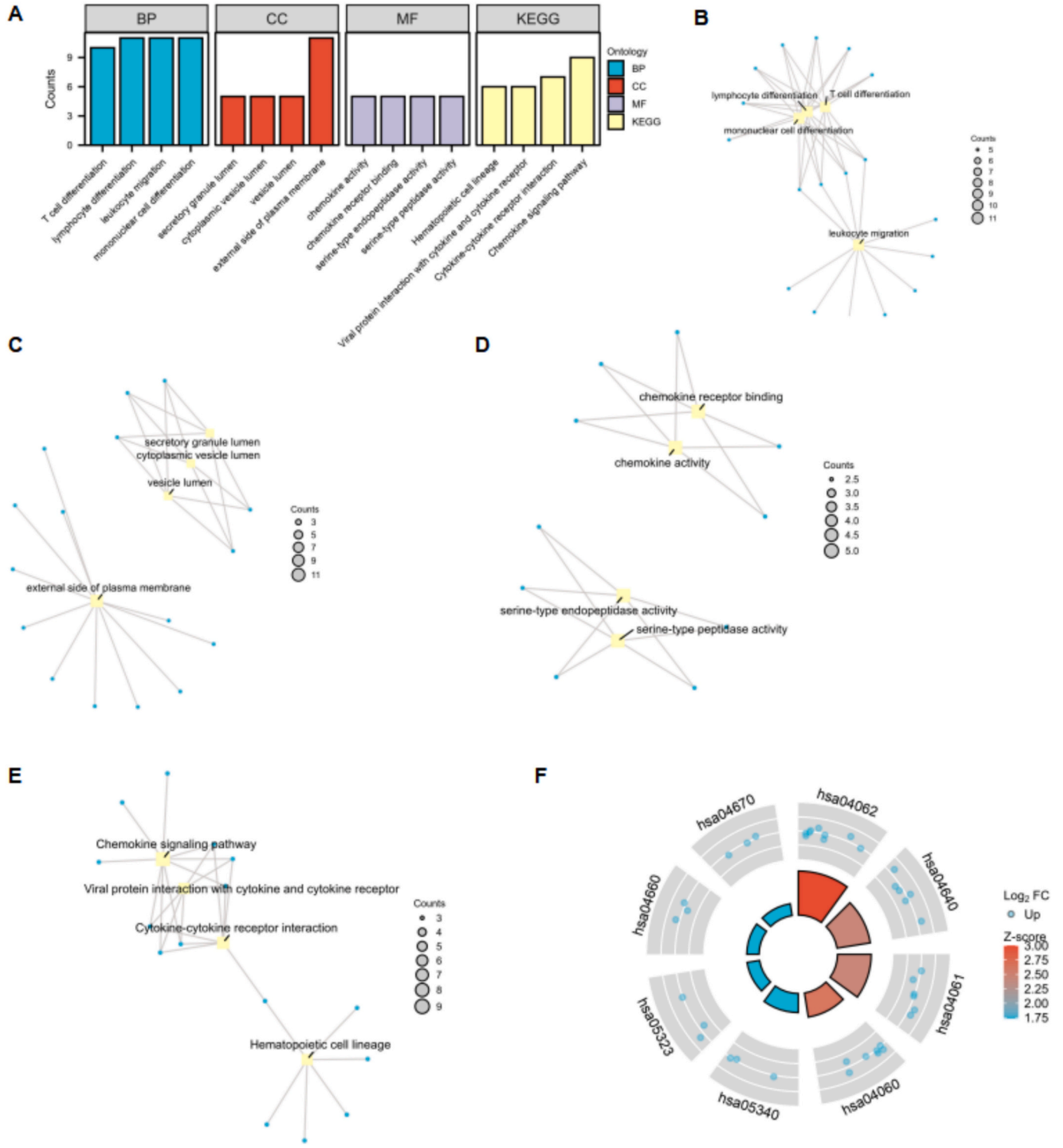

Fig. 3. GO and KEGG pathway enrichment analysis of DEGs. DEGs were functionally annotated and analyzed for pathway enrichment using GO and KEGG analyses. The overall enrichment results are summarized in the bar plot (A). GO terms, including BP, CC, and MF, are visualized as network diagrams in panels B—D. KEGG pathway analysis results are presented as a network plot and a circular diagram in panels E and F, respectively.

responses. The visual distribution of the gene sets reinforces their functional relevance in fibrosis, highlighting the dominant enrichment of immune signaling modules. In Fig. 4C, we focused on the nine most significantly enriched pathways, selected based on FDR < 0.25 and Benjamini-Hochberg (BH) adjusted p-value <0.05. These included: REACTOME_IMMUNOREGULATORY_INTERACTIONS_BETWEEN_A_LYMPHOID_AND_A_NON_LYMPHOID_CELL, which describes the cellular crosstalk between lymphoid and non-lymphoid cells—critical in initiating immune responses and shaping the tissue immune microenvironment. REACTOME_CHEMOKINE_RECEPTORS_BIND_CHEMOKINES, highlighting the core process of chemokine–receptor interactions that regulate immune cell trafficking during inflammation and fibrosis. REACTOME_INTERFERON_SIGNALING, REACTOME_INTERFERON_GAMMA_SIGNALING, and

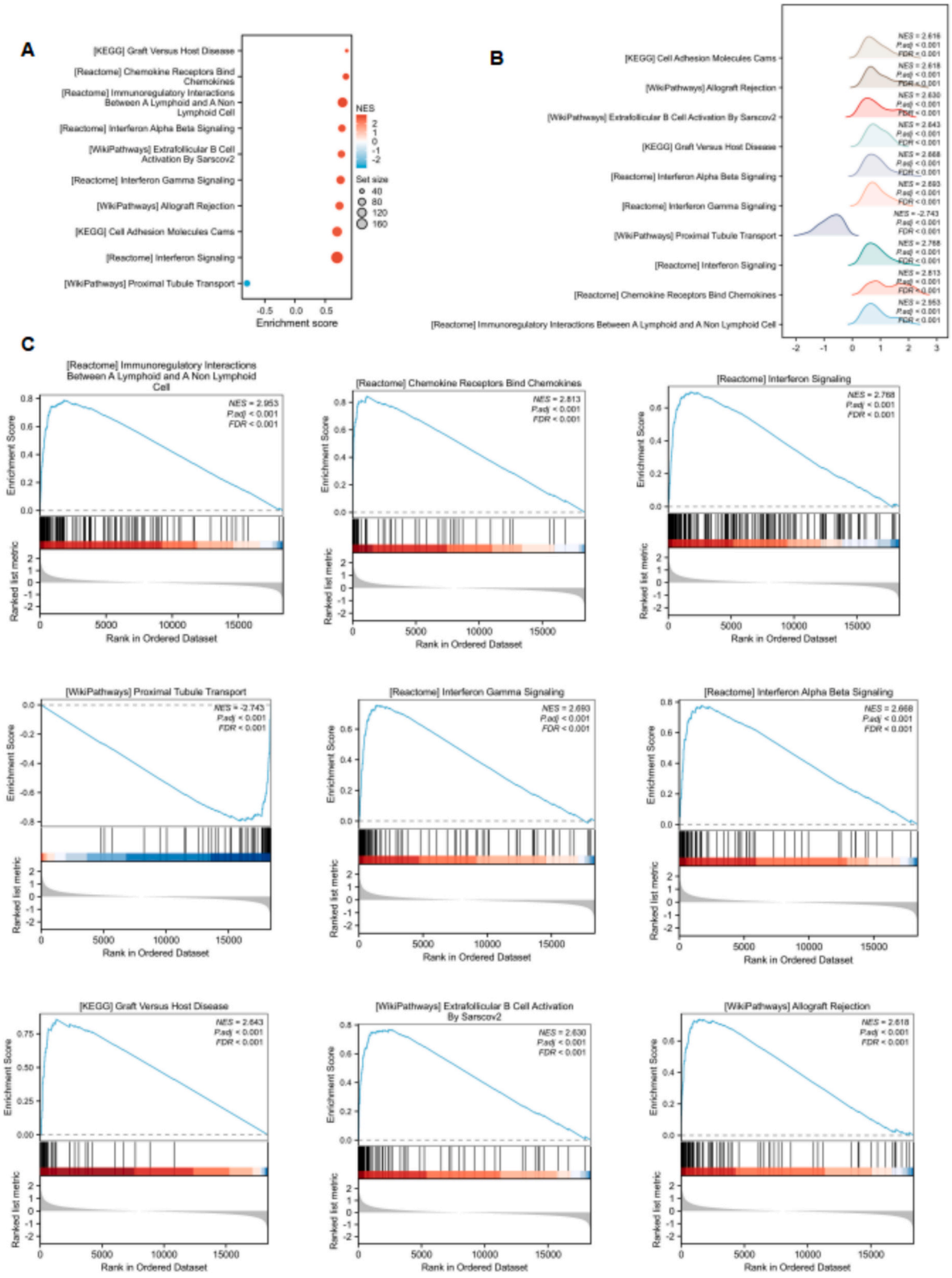

Fig. 4. GSEA analysis of DEGs. GSEA was conducted on the integrated dataset to identify enriched biological processes associated with gene expression, as well as to characterize affected cellular components and molecular functions. The top ten enriched biological functions are illustrated in a bubble plot (Figure A) and a ridge plot (Figure B). A subset of nine representative pathways with the most significant enrichment is visualized in Figure C, selected based on the criteria of a FDR < 0.25 and a BH adjusted p-value <0.05. In the bubble plot, the size of each bubble reflects the number of genes enriched in the corresponding pathway, while the color indicates the NES, with warmer colors (e.g., red) representing higher NES values and cooler colors (e.g., blue) representing lower values. All GSEA results were evaluated using adjusted *p*-values and FDR thresholds, with multiple testing correction performed using the BH method. (For interpretation of the references to color in this figure legend, the reader is referred to the web version of this article.)

REACTOME_INTERFERON_ALPHA_BETA_SIGNALING, representing three distinct interferon-mediated pathways that are closely linked to antiviral responses, immune cell activation, and antifibrotic regulation. WP_PROXIMAL_TUBULE_TRANSPORT, which encompasses physiological functions of proximal tubule cells, including reabsorption of water, electrolytes, nutrients, and waste products—fundamental to maintaining renal homeostasis. KEGG_GRAFT_VERSUS_HOST_DISEASE and WP_ALLOGRAFT_REJECTION, both reflecting immune activation pathways akin to transplant immunopathology, suggesting potential immune rejection-like mechanisms in fibrosis progression. WP_EXTRAFOLLICULAR_B_CELL_ACTIVATION_BY_SARSCOV2, pointing to potential intersections between viral-induced B cell responses and fibrotic immune pathology. Collectively, the GSEA results are highly consistent with the immune activation patterns observed in the prior GO

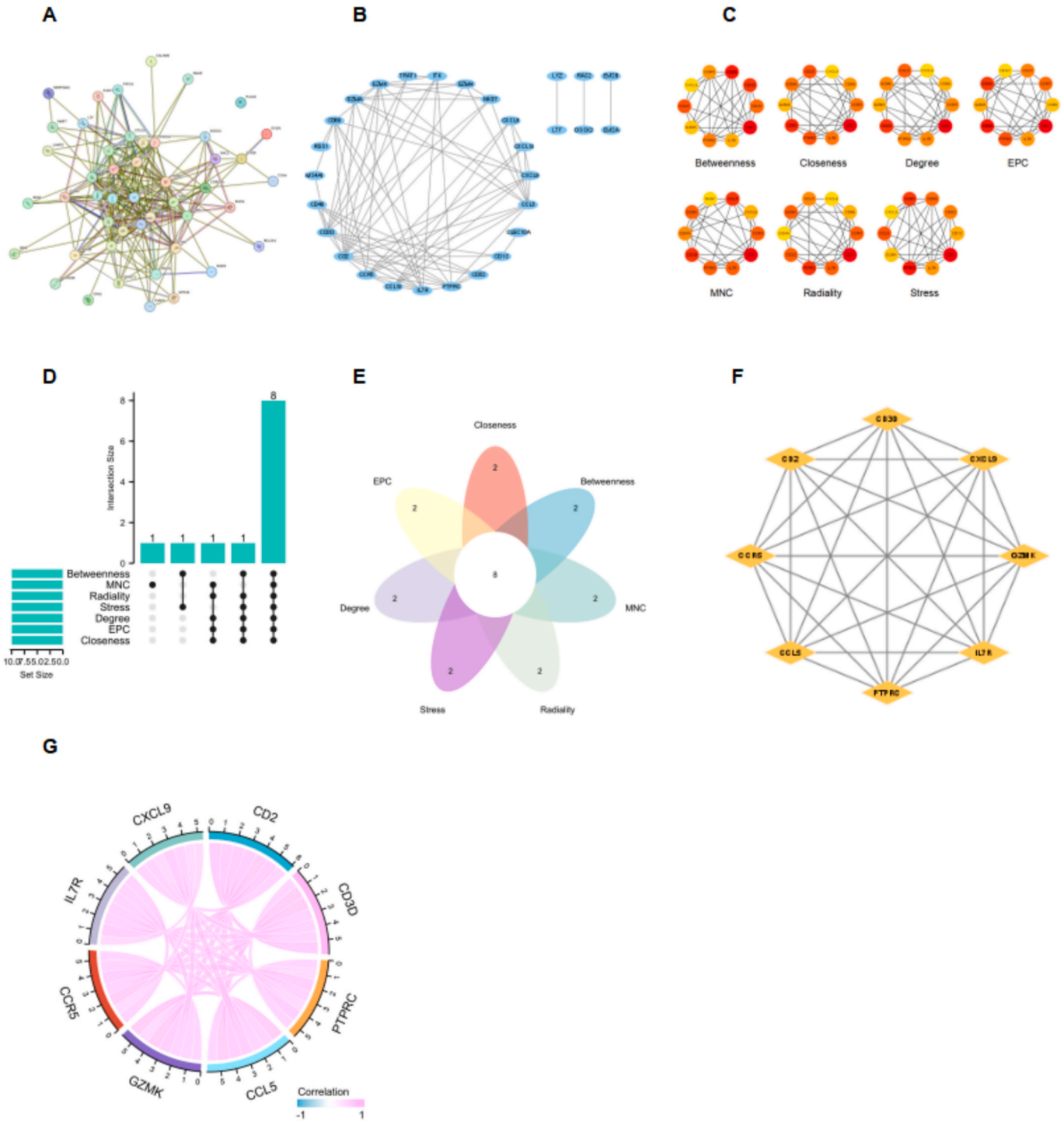

Fig. 5. PPI network analysis and identification of hub genes. The PPI network of DEGs was constructed using the STRING database (Figure A). The resulting network was visualized in Cytoscape (Figure B), and key hub genes were identified using the CytoHubba plugin, applying seven topological algorithms to rank the top 10 genes from each method (Figure C). An UpSet plot (Figure D) and a petal diagram (Figure E) were used to identify the intersection of these rankings, resulting in the selection of eight core hub genes. The PPI network of these eight hub genes was further visualized using Cytoscape (Figure F), and their pairwise interactions were illustrated in a chord diagram (Figure G), providing a comprehensive view of their interconnectivity and potential cooperative roles in disease progression.

and KEGG analyses. These findings further confirm that renal interstitial fibrosis is characterized by robust inflammatory responses, immune cell infiltration, and complex immunoregulatory signaling networks. The results strengthen the rationale for targeting the immune microenvironment as a therapeutic strategy in the treatment of renal interstitial fibrosis.

3.4. PPI network construction and identification of key hub genes

To further explore the potential roles of DEGs in RIF, we conducted a PPI network analysis. This approach aimed to elucidate the interaction landscape among DEGs and to identify hub genes that may play central roles in disease progression. As shown in Fig. 5A, we first constructed the PPI network using the STRING database. The resulting network comprised 47 nodes and 260 edges, with an average node degree of 11.1, indicating a highly interconnected structure among the encoded proteins. Fig. 5B presents a Cytoscape visualization of the PPI network, providing an intuitive representation of the interrelationships between the DEGs and facilitating the identification of core genes potentially involved in renal fibrosis. To systematically screen for key regulatory genes, we used the CytoHubba plugin in Cytoscape, as shown in Fig. 5C. Seven topological algorithms—Betweenness, Closeness, Degree, EPC, MNC, Radiality, and Stress—were applied to rank the top 10 genes from each method based on their importance within the network. These algorithms evaluate centrality from different perspectives, enhancing the robustness of hub gene identification. Fig. 5D and 5E display the overlap

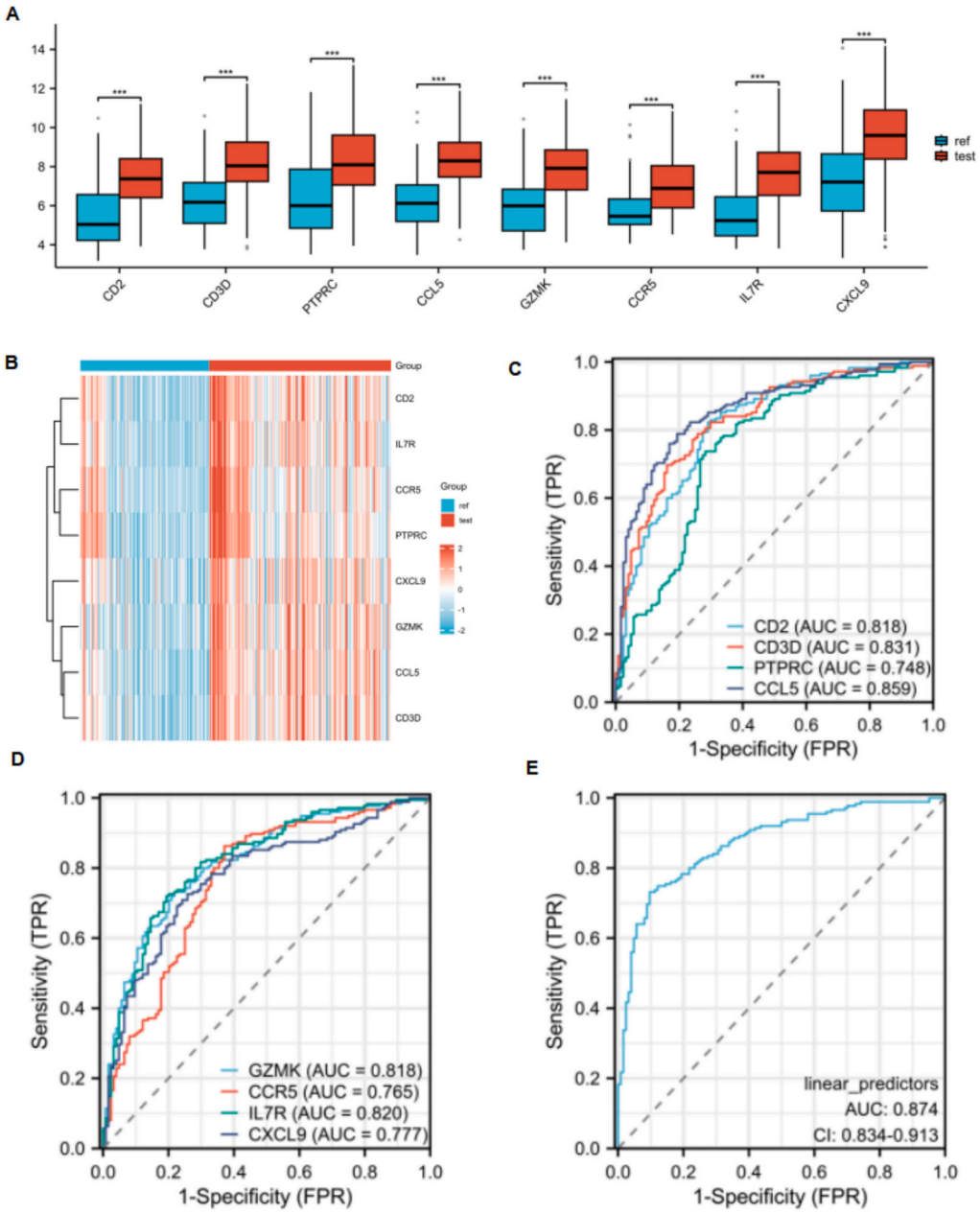

Fig. 6. Validation of hub gene expression and ROC curve analysis. Expression of the eight identified hub genes was validated in renal interstitial fibrosis patients by merging two datasets and conducting group comparison analysis (Figure A). The results showed significant upregulation in the fibrosis group, with $p < 0.1$ and $^{**}p < 0.01$ indicating levels of statistical significance. The overall expression profiles of the eight hub genes in the combined dataset are displayed as a heatmap in Figure B. ROC curve analysis was performed for each gene (Figures C and D) to assess their diagnostic performance in renal interstitial fibrosis, including CD2, CD3D, PTPRC, CCL5, CCR5, GZMK, IL7R, and CXCL9. Based on an AUC threshold of >0.75, seven hub genes were selected to construct a logistic regression model. As shown in Figure E, this multigene model demonstrated strong diagnostic performance in the combined dataset, with an AUC of 0.874.

of top-ranked genes identified by the seven algorithms using an UpSet plot and a petal diagram, respectively. Through this integrative analysis, eight consensus hub genes were identified: CD2, CD3D, PTPRC, CXCL9, IL7R, CCL5, CCR5, and GZMK. These genes are likely to play critical roles in mediating immune responses associated with renal interstitial fibrosis. The final PPI network of these eight hub genes is visualized in Fig. 5F, illustrating their tight interconnections. Fig. 5G further presents a chord diagram depicting the pairwise interactions among these hub genes, emphasizing their potential as core regulators in the fibrotic process. Overall, this PPI network analysis and hub gene screening highlight a tightly connected immune-related gene module, reinforcing the notion that immune dysregulation is a key driver in the pathogenesis of renal interstitial fibrosis.

3.5. Validation of hub gene expression and diagnostic potential in renal interstitial fibrosis

Following the identification of eight key hub genes through PPI network analysis, we further evaluated their expression levels and diagnostic potential in renal interstitial fibrosis. To ensure robustness, we merged the GSE22459 and GSE76882 datasets, comprising a total of 124 control samples and 175 renal interstitial fibrosis samples. The expression levels of the eight hub genes were then systematically validated. Fig. 6A presents the differential expression levels of the eight hub genes between fibrosis and control groups. All eight genes were significantly upregulated in renal interstitial fibrosis samples compared to controls ($p < 0.01$), reinforcing their potential functional roles in disease progression. Fig. 6B displays a heatmap of these genes across the combined dataset, clearly illustrating distinct expression patterns between fibrotic and non-fibrotic tissues. To explore their diagnostic utility, we conducted ROC curve analysis for each gene. Fig. 6C and 6D show that all eight genes achieved an area under the curve (AUC) greater than 0.70, indicating moderate to high diagnostic accuracy. Among them, CCL5 demonstrated the highest AUC (0.859), suggesting strong discriminatory power. Other genes with high diagnostic performance included CD3D (AUC = 0.831), IL7R (0.820), CD2 (0.818), and GZMK (0.818). CXCL9 (0.777) and CCR5 (0.765) also exhibited acceptable diagnostic efficacy, while PTPRC showed a lower AUC of 0.748, though still within an acceptable range. Based on these findings, we developed a logistic regression model incorporating the top seven performing hub genes (AUC > 0.75, excluding PTPRC). As shown in Fig. 6E, the multigene model achieved a combined AUC of 0.874 (95 % CI: 0.834–0.913), significantly outperforming any single gene in isolation. This suggests that a composite gene panel offers superior diagnostic sensitivity and specificity for renal interstitial fibrosis. In summary, these seven hub genes are not only differentially expressed in fibrotic tissues but also possess strong diagnostic potential. The development of a multigene logistic model underscores the promise of these genes as a noninvasive molecular biomarker panel for early detection and diagnosis of renal interstitial fibrosis.

3.6. Validation of hub gene expression in mouse and human samples and their roles in renal interstitial fibrosis

Building on the PPI network analysis and hub gene identification from human transcriptomic datasets, we observed that seven hub genes were significantly upregulated in renal interstitial fibrosis. To further validate their functional roles, we performed experimental analyses in a mouse model. Fig. 7A shows Masson's trichrome staining of kidney tissues from sham-operated (Sham) and unilateral ureteral obstruction (UUO) mice. The UUO group exhibited pronounced collagen deposition, confirming successful establishment of renal interstitial fibrosis in this model. We next assessed the mRNA expression of the seven hub genes (CD3D, CCL5, CD2, CCR5, IL7R, CXCL9, and GZMK) using qPCR in the same mouse samples. As shown in Fig. 7B, six genes—CD3D, CCL5, CD2, CCR5, IL7R, and CXCL9—were significantly upregulated in the UUO group compared to controls, further supporting their involvement in fibrosis progression. Given the diagnostic performance and qPCR expression differences of CD3D and CCL5, we further evaluated their protein levels via Western blot. Fig. 7C demonstrates markedly increased protein expression of CD3D and CCL5 in UUO mice. Quantitative analysis in Fig. 7D confirmed that these changes were statistically significant. To assess whether these findings translate to humans, Fig. 7E displays Masson's trichrome staining of kidney biopsies from patients with stage 1 and stage 5 CKD. Stage 5 CKD kidneys showed markedly increased fibrosis and collagen accumulation. In Fig. 7F, immunofluorescence staining of human kidney tissues confirmed elevated CD3D and CCL5 expression in fibrotic kidneys, implicating their roles in immune activation and tissue remodeling in human renal fibrosis. Taken together, transcriptomic analysis and experimental validation consistently support that the hub genes—particularly CD3D and CCL5—are critically involved in renal interstitial fibrosis. These genes not only demonstrated consistent upregulation across species but also represent promising targets for future clinical investigation and potential therapeutic intervention.

3.7. Regulatory network analysis of hub genes: mRNA–miRNA and mRNA–TF interactions

Following experimental validation of hub genes (CD3D, CCL5, CD2, CCR5, IL7R, CXCL9) in both mouse models and human samples, we sought to further elucidate their upstream regulatory mechanisms. To construct a comprehensive molecular regulatory framework underlying renal interstitial fibrosis, we systematically predicted miRNA and TF interactions using multiple databases and visualized the regulatory networks. In Fig. 8A, the mRNA–miRNA interaction network was constructed using predictions from the StarBase database and visualized with Cytoscape. The resulting network revealed potential regulatory relationships between 2 hub genes and 34 miRNAs, forming a complex regulatory topology. Fig. 8B shows independently predicted interactions from the TargetScan database, identifying 2 miRNAs associated with 2 hub genes. This cross-database overlap further supports the reliability of miRNA-mediated regulation. Additional predictions from miRDB and miRTarBase are presented in Fig. 8C and 8D, revealing interactions of 73 and 61 miRNAs with 4 and 5 hub genes, respectively. These networks emphasize the multifactorial and layered nature of miRNA regulation in renal interstitial fibrosis, where multiple miRNAs may coordinately modulate hub gene expression. To enhance confidence in the predicted interactions, we integrated results from all four databases (StarBase, TargetScan, miRDB, and miRTarBase), retaining only those miRNAs identified in at least two sources (Fig. 8E). The resulting consensus network revealed that hsa-miR-619-5p, hsa-miR-671-5p, hsa-miR-7151-3p, and hsa-miR-5194 may regulate CCL5, while hsa-miR-370-3p may target CD3D. These miRNAs are likely to function as key upstream regulators in the fibrotic process. To explore transcriptional regulation, we integrated data from multiple TF prediction platforms to build an mRNA–TF interaction network (Fig. 8F). In the network, hub genes are indicated in dark green, and TFs in light green. The results suggest that: IL7R may be co-regulated by SPI1, RUNX1, FOS, and RELA; CCL5 may be modulated by RELA, SPI1, and RUNX1; CXCL9 appears to be regulated by RELA and ERG; CD3D is potentially influenced by multiple TFs including FOXA1, ERG, GABPA, ELF1, CREB1, CEBPB, NRF1, AR, MAX, SPI1, ETS1, HOXB13, and MYC. These TFs may exert either activating or repressive control over hub gene expression, affecting downstream biological processes such as cell proliferation, migration, and differentiation.Together, the integrative mRNA–miRNA and mRNA–TF network analyses provide mechanistic insights into the regulation of fibrosis-associated hub genes in both murine and human contexts. These findings not only offer molecular-level explanations for the observed gene expression patterns in wet-lab experiments but also present new potential targets for therapeutic intervention in renal interstitial fibrosis.

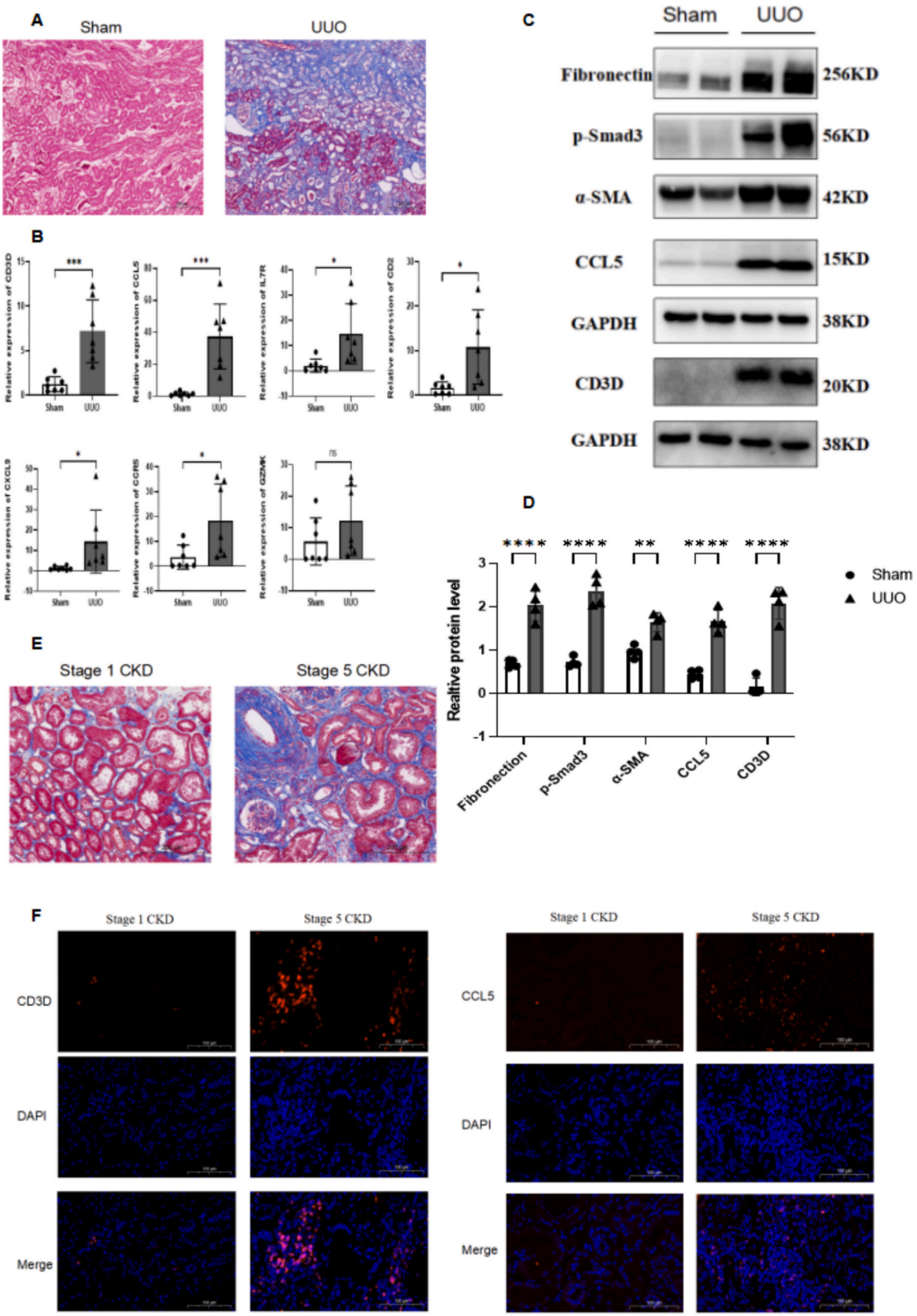

Fig. 7. In vivo validation of hub gene expression. Mouse tissue sections were subjected to Masson's trichrome staining (Figure A), followed by RNA extraction from renal tissues and quantitative real-time PCR (Figure B) to assess the expression levels of seven key genes in a mouse model of renal interstitial fibrosis. Among the genes, CCL5 and CD3D exhibited the most significant differential expression. Based on these findings, Western blot analysis (Figure C) and protein quantification (Figure D) were performed on renal tissues from the mice. Additionally, Masson's trichrome staining was applied to kidney tissue sections from clinical Stage 1 and Stage 5 CKD patients (Figure E), and immunofluorescence staining for CD3D and CCL5 was conducted on patient tissue samples (Figure F).

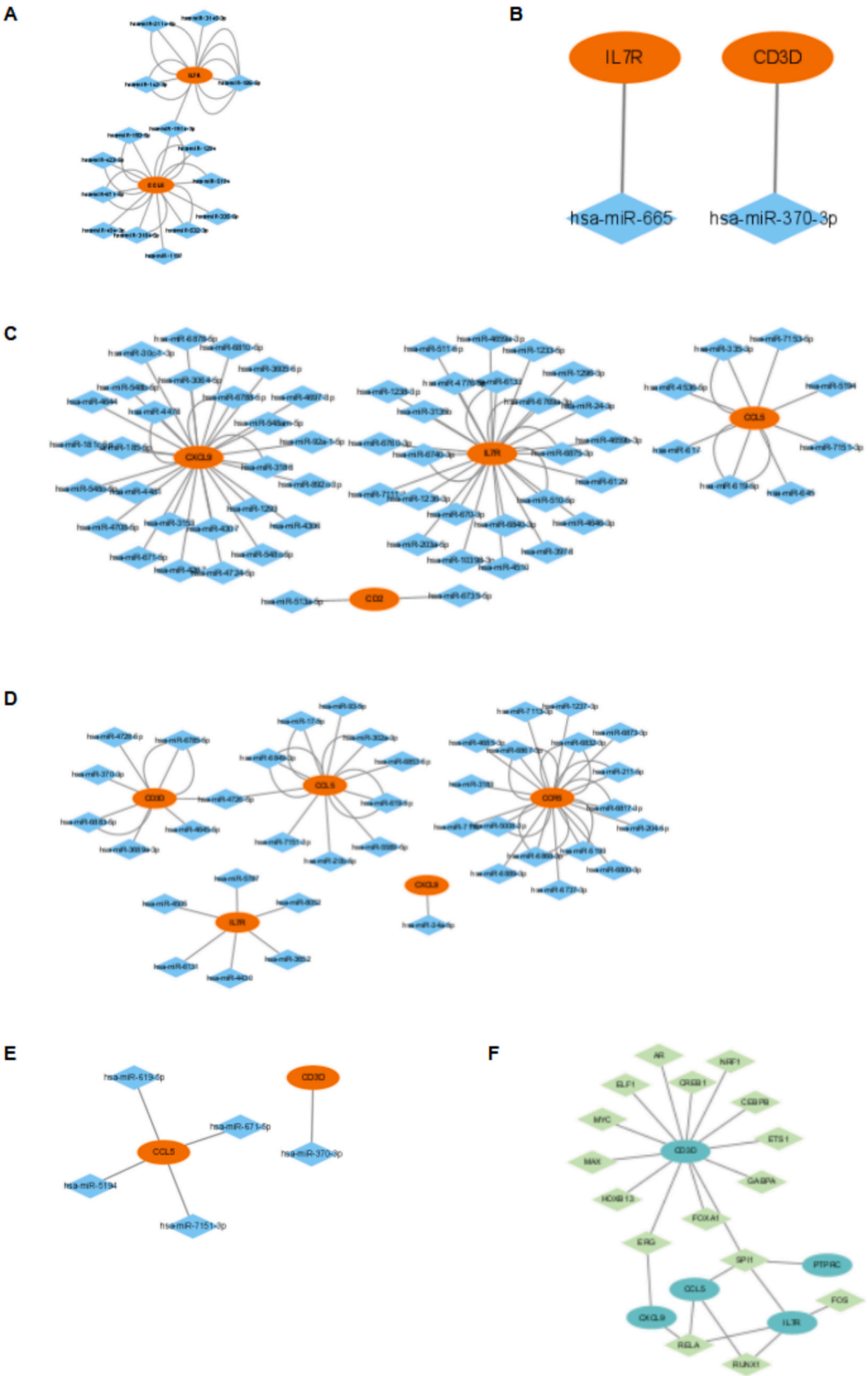

Fig. 8. Regulatory network analysis of hub genes involving mRNA–miRNA and mRNA–TF interactions. MicroRNAs potentially regulating the identified hub genes were predicted using four databases: StarBase (Figure A), TargetScan (Figure B), miRDB (Figure C), and miRTarBase (Figure D). mRNA–miRNA regulatory networks were constructed based on each database and visualized using Cytoscape. To improve reliability, miRNAs that were co-predicted by at least two of the four databases were selected and integrated into a consensus mRNA–miRNA regulatory network (Figure E), also visualized using Cytoscape. Additionally, Figure F illustrates the mRNA–TF regulatory network, highlighting the transcriptional regulation landscape of the hub genes.

3.8. Immune cell infiltration analysis reveals key molecular mechanisms in renal interstitial fibrosis

To elucidate the immune regulatory roles potentially mediated by the identified hub genes in renal interstitial fibrosis, we conducted a systematic immune cell infiltration analysis using the single-sample Gene Set Enrichment Analysis (ssGSEA) algorithm, followed by correlation assessments between immune cell abundance and hub gene expression. Fig. 9A displays the immune infiltration differences between fibrotic and control groups, as assessed by Wilcoxon tests. A total of 24 immune cell types showed significantly altered abundance ($p < 0.05$), suggesting immune activation within the fibrotic microenvironment. The ssGSEA-based immune cell abundance heatmap is shown in Fig. 9B, illustrating distinct infiltration patterns between groups. To identify the most functionally relevant immune cell subtypes under fibrotic conditions, we performed LASSO regression analysis (Figs. 9C and 9D). The model identified cytotoxic cells, dendritic cells, mast cells, NK cells, T cells, and Th17 cells as having the highest feature weights, indicating their prominent involvement in the fibrotic niche. Correlation analysis of immune infiltration levels (Fig. 9E) revealed strong positive relationships ($r > 0.5$) among several immune subsets, particularly between cytotoxic cells and T cells ($r = 0.88$, $p < 0.05$), activated dendritic cells (aDCs) and T cells ($r = 0.82$, $p < 0.05$), and aDCs with cytotoxic cells ($r = 0.82$, $p < 0.05$). These results (Fig. 9F) suggest coordinated infiltration and potential functional synergy in immune dysregulation and tissue injury. We next evaluated the correlations between hub gene expression and immune cell infiltration. A heatmap summarizing these associations is shown in Fig. 9G, while representative gene–immune cell interactions are illustrated in Fig. 9H via scatter plots. Multiple hub genes exhibited strong positive correlations with T cell subpopulations, dendritic cells, and NK cells, implying significant roles in immune cell recruitment and activation. In particular, CD3D and CCL5 emerged as central immune-associated genes: CD3D showed strong positive correlations with total T cells ($r = 0.946$), cytotoxic cells ($r = 0.891$), aDCs ($r = 0.802$), Th1 cells ($r = 0.714$), and B cells ($r = 0.703$), suggesting a key role in T cell–mediated adaptive immunity and proinflammatory amplification. CCL5, a known chemokine, was highly correlated with T cells ($r = 0.910$), cytotoxic cells ($r = 0.909$), aDCs ($r = 0.813$), and Th1 cells ($r = 0.715$), supporting its function in recruiting proinflammatory T cells and dendritic cells to sites of inflammation. Other hub genes also demonstrated relevant immune associations: CD2 correlated strongly with T cells ($r = 0.929$) and cytotoxic cells ($r = 0.896$), indicating involvement in T cell recognition and co-stimulation. CXCL9 was most strongly associated with cytotoxic cells ($r = 0.849$) and aDCs ($r = 0.842$), consistent with its role in interferon-mediated immune responses. IL7R was positively associated with T cells ($r = 0.864$) but negatively correlated with regulatory T cells (Tregs; $r = -0.528$), suggesting dual roles in immune activation and tolerance. CCR5 showed positive associations with cytotoxic cells ($r = 0.842$) and Th1 cells ($r = 0.836$), aligning with its function in directing T cell chemotaxis. These findings demonstrate that the hub genes—especially CD3D and CCL5—are tightly linked to immune cell infiltration, potentially playing pivotal roles in T cell activation and proinflammatory cell recruitment. The integrated analysis provides strong evidence for immune system involvement in the pathogenesis of renal interstitial fibrosis and reveals a complex regulatory landscape between immune cells and fibrotic gene programs.

3.9. Potential drug targeting of key hub genes and molecular docking validation

To further explore the therapeutic potential of key hub genes in renal interstitial fibrosis, we performed target prediction analyses for six core genes (CCL5, CD3D, CCR5, IL7R, CD2, and CXCL9) using the Coremine Medical database. This approach identified a series of known drugs and natural compounds with potential interactions with these genes. The drug–gene interaction networks were visualized in Fig. 10A and 10B, highlighting the distribution of candidate compounds targeting each hub gene. These included clinically relevant molecules such as TAK-779, interferon-gamma, triciribine, and traditional medicine-related agents like recombinant interleukin-6. To validate the binding capacity between candidate drugs and their targets, we conducted molecular docking simulations. Binding energy was used as the primary index for interaction affinity: values below 0 kcal/mol were considered to indicate binding activity, while values below −5 kcal/mol suggested strong binding affinity. All candidate compounds showed negative binding energies, suggesting favorable interaction potential. For each hub gene, we selected the drug with the lowest binding energy for three-dimensional docking and interaction modeling. As shown in Fig. 10C—H, all selected drug–target pairs formed stable binding conformations with good spatial complementarity and hydrogen bonding potential. Specific findings include: CCL5 formed multiple hydrogen bonds with recombinant interleukin-6, showing the lowest binding energy among all pairs. CCR5 exhibited strong hydrophobic complementarity and hydrogen bonding with the small molecule antagonist TAK-779. CD2 displayed a strong electrostatic interaction interface with interferon-gamma. CD3D bound stably to triciribine, with a clearly defined binding pocket. CXCL9 also interacted favorably with recombinant interleukin-6, exhibiting excellent binding free energy. IL7R formed multiple hydrogen bonds with the camptothecin analogue TLC388, indicating a strong and specific interaction. These binding modes were further annotated based on hydrogen bond count and interaction distance, providing a detailed visualization of drug–target interfaces. Collectively, these results offer molecular-level evidence supporting the druggability of key hub genes in renal interstitial fibrosis. The identified small-molecule candidates and their structural binding characteristics provide a foundation for the rational design of targeted therapies against fibrotic kidney disease.

4. Discussion

In this study, we systematically identified and validated key molecular mechanisms and potential therapeutic targets in RIF by integrating transcriptomic data, bioinformatic analyses, immune infiltration profiling, regulatory network construction, and molecular docking simulations. Central to our findings are six hub genes—CCL5, CD3D, CCR5, IL7R, CD2, and CXCL9—which are closely associated with immune responses, cell migration, and immune evasion. These genes were comprehensively analyzed across three dimensions: regulatory networks, immune infiltration characteristics, and drug–target relationships, with particular emphasis on the central roles of CD3D and CCL5 in modulating immune cell function. Differential expression analysis confirmed that all six hub genes are significantly upregulated in fibrotic renal tissue, suggesting their potential involvement in disease initiation and progression. PPI network construction further revealed that these genes occupy central positions within the interaction network, with markedly higher average node degrees, reinforcing their roles as core regulatory elements. Functional enrichment analyses (GO and KEGG) indicated that these genes are predominantly enriched in immune-related biological processes and signaling pathways, including T cell activation, cytokine–cytokine receptor interactions, and the chemokine signaling pathway, implying that they may influence fibrosis through immune cell modulation. Immune infiltration analysis using the ssGSEA algorithm demonstrated substantial enrichment of immune cell subpopulations—including $CD8^+$ T cells, Th1 cells, dendritic cells, natural killer (NK) cells, and regulatory T cells—in fibrotic tissue. LASSO regression analysis identified CD3D and CCL5 as highly co-expressed with multiple key immune subsets. Visualization analyses further clarified that CD3D is positively correlated with Th1 cells, activated dendritic cells (aDCs), and $CD8^+$ T cells, while CCL5 shows strong coupling with Th1 cells, total T cells, and NK cells. Together, these data delineate a pro-inflammatory immune regulatory network centered around the

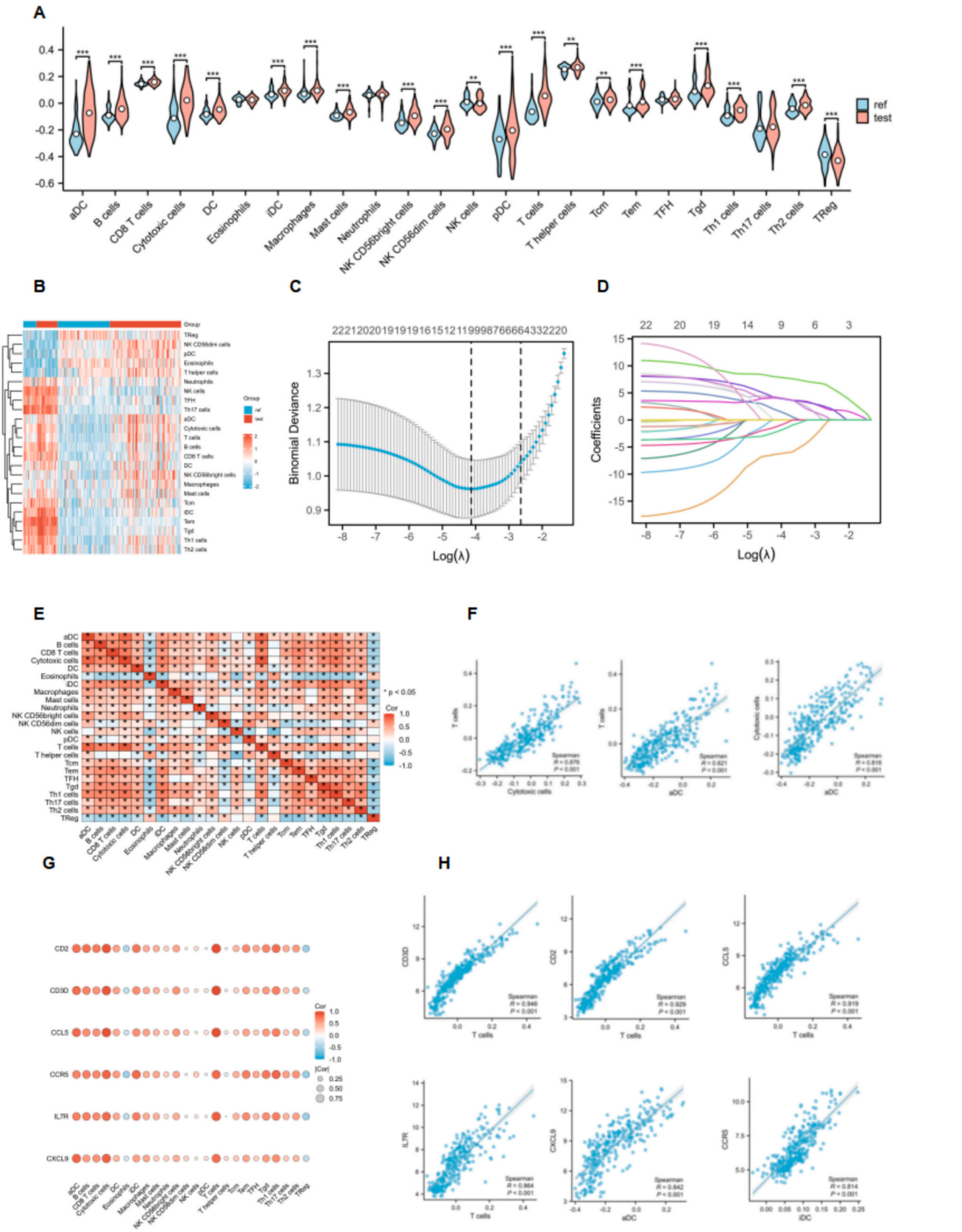

(caption on next page)

Fig. 9. Immune cell infiltration analysis using the ssGSEA algorithm. Immune cell infiltration in the merged dataset was analyzed using ssGSEA. A group comparison plot (Figure A) illustrates the integrated immune cell infiltration profiles between renal interstitial fibrosis samples (orange) and control samples (blue). The relative infiltration levels of 24 immune cell types are shown in a heatmap (Figure B). LASSO regression analysis (Figures C and D) was applied to identify immune cell types most relevant to fibrosis status. Correlations among immune cell types are presented in a heatmap (Figure E), where red indicates positive correlation and blue indicates negative correlation, with color intensity reflecting correlation strength. Strongly correlated immune cell pairs were further visualized using scatter plots (Figure F). The relationships between hub genes and immune cell infiltration were summarized in a heatmap (Figure G), and for each hub gene, the most strongly correlated immune cell type was displayed as an individual scatter plot (Figure H). Statistical significance is indicated as follows: *ns* (not significant): $p \geq 0.05$; *: $p < 0.05$ (significant) ; **: $p < 0.01$ (highly significant) ; ***: $p < 0.001$ (very highly significant). The absolute value of Pearson's correlation coefficient (r) denotes the strength of the association: $|r| < 0.3$: negligible or weak correlation; $0.3 \leq |r| < 0.5$: weak correlation; $0.5 \leq |r| < 0.8$: moderate correlation; $|r| \geq 0.8$: strong correlation. Red in correlation heatmaps indicates a positive relationship, blue indicates a negative one, and color intensity corresponds to the strength of the association. (For interpretation of the references to color in this figure legend, the reader is referred to the web version of this article.)

CD3D–CCL5 axis, which may serve as a key functional module sustaining local immune activation and driving fibrotic cascades. This discovery not only enhances our understanding of the immune pathogenesis of RIF but also provides a theoretical basis for the development of targeted therapeutic strategies.

CD3D, as an essential component of the T cell receptor (TCR) complex, plays a non-redundant role in T cell activation, proliferation, and adaptive immune responses, and its function has gained increasing attention in the context of inflammatory diseases and tissue remodeling [21]. In this study, we found that CD3D was significantly upregulated in renal interstitial fibrosis (RIF) tissues and was highly correlated with multiple immune cell types, especially total T cells ($r = 0.946$), cytotoxic T cells ($r = 0.891$), activated dendritic cells (aDCs, $r = 0.802$), Th1 cells ($r = 0.714$), and B cells ($r = 0.703$). These results suggest that CD3D is not only central to T cell activation but may also act as a key modulator of the local renal inflammatory microenvironment. From a pathophysiological standpoint, the upregulation of CD3D may promote persistent T cell activation within the kidney, enhancing the release of pro-inflammatory cytokines such as IFN-γ and IL-17, which are known to play pivotal roles in driving renal fibrosis [22]. Upon recognition of antigens presented by antigen-presenting cells (APCs) via MHC complexes and engagement of the TCR/CD3 complex, T cells release chemokines that recruit monocytes, dendritic cells, and other effector cells to the site of inflammation, exacerbating immune responses and triggering fibroblast activation and myofibroblast differentiation—ultimately leading to collagen deposition and extracellular matrix remodeling. In our analysis, CD3D showed strong co-expression with aDCs and Th1 cells, further supporting its potential role as a bridge in intercellular immune signaling and inflammation amplification. Previous studies also highlight CD3D as a key player in other fibrotic diseases. For example, in patients with non-alcoholic steatohepatitis (NASH), CD3D-high T cells were found to be enriched in fibrotic liver regions and proposed as biomarkers for disease progression [23]. Conversely, CD3D downregulation has been associated with impaired immune function and poor clinical outcomes [24]. In sepsis, decreased CD3D expression caused by impaired antigen presentation correlates with reduced immune surveillance [25]. In diabetic nephropathy, CD3D has been shown to activate the JAK/STAT signaling pathway, thereby exacerbating glucose-induced cellular stress; silencing CD3D significantly alleviated renal injury and reduced inflammatory cytokine levels, underscoring its role as a central regulator of inflammatory damage [26]. Taken together, our findings suggest that CD3D may amplify T cell-mediated immune responses in RIF, sustaining inflammation and promoting fibroblast and myofibroblast recruitment. T cells may activate immune responses via CD3D by interacting with APCs and releasing cytokines such as IFN-γ and IL-17, thereby promoting mesenchymal transition and fibrotic remodeling [9]. Additionally, CD3D appears to be subject to multilayered regulation. At the post-transcriptional level, miR-370-3p was predicted as a potential regulatory miRNA, suggesting a role in modulating CD3D mRNA stability and translation. At the transcriptional level, multiple immune-related transcription factors—including FOXA1, ERG, GABPA, ELF1, CREB1, CEBPB, NRF1, AR, MAX, SPI1, ETS1, HOXB13, and MYC—were identified as putative upstream regulators, positioning CD3D at the convergence of multiple inflammatory signaling pathways and feedback circuits. Finally, our molecular docking results provide theoretical support for CD3D as a potential drug target. Structural modeling revealed that the small-molecule compound Triciribine binds stably to CD3D, with favorable spatial complementarity and low binding free energy—suggesting its potential as an immune-modulatory therapeutic candidate in fibrosis.

CCL5 (also known as RANTES), a classical pro-inflammatory chemokine, has been widely implicated as a key mediator in various fibrotic diseases. In the context of RIF, it plays a pivotal role in shaping the inflammatory microenvironment and promoting fibrotic remodeling by orchestrating immune cell recruitment, activation, and tissue localization [27]. CCL5 primarily binds to the CCR5 receptor, directing the chemotaxis of multiple immune cell types—including T cells, monocytes/macrophages, dendritic cells, and eosinophils—toward inflamed tissue, thereby amplifying the local immune response [28]. In our study, CCL5 was found to be significantly upregulated in RIF tissue and exhibited strong positive correlations with the infiltration levels of several key immune cell subsets, including T cells, cytotoxic T cells, aDCs, and Th1 cells. This supports its functional role as a regulatory hub for immune cell migration and suggests it may serve as a molecular initiator of the fibrotic microenvironment. Beyond chemotaxis, CCL5 can also activate multiple signaling pathways that promote the expression of fibrosis-related cytokines and markers. Notably, CCL5 is capable of activating the NF-κB pathway, a central inflammatory axis that induces a cascade of inflammatory cytokines and adhesion molecules, thereby sustaining and amplifying inflammation. In myocardial fibrosis models, CCL5 was shown to induce extensive cytokine secretion via the NF-κB pathway and promote immune cell accumulation at sites of cardiac injury, while pharmacological antagonism significantly reduced infarct size and inflammation [29]. A similar mechanism is likely applicable to renal tissue, where persistent CCL5 signaling may stimulate fibroblast activation via the NF-κB or MAPK/ERK pathways, drive myofibroblast differentiation, and enhance the synthesis of extracellular matrix proteins such as type I collagen, thereby advancing the fibrotic process. In both experimental and clinical models of diabetic nephropathy and tubulointerstitial fibrosis, CCL5 expression is consistently elevated, particularly within the renal interstitium, and closely correlates with macrophage infiltration [30]. Wada et al. [31] demonstrated that CCL5-mediated recruitment of monocytes and macrophages via CCR5 contributes to local inflammatory amplification and tissue damage; the use of neutralizing antibodies significantly reduced fibrosis [32], reinforcing its functional importance in renal fibrogenesis. Moreover, CCL5 has been shown to upregulate fibrotic markers such as α-SMA and fibronectin through the ERK signaling pathway, while antibody blockade attenuates their expression, suggesting a role in maintaining the fibrotic phenotype [33]. Additionally, CCL5 can recruit diverse immune cells (e.g., T cells, dendritic cells, eosinophils) via its interaction with three distinct G protein–coupled receptors, thereby exacerbating fibrosis. In liver fibrosis, CCL5 is recognized as a key mediator, and its receptor antagonists have demonstrated therapeutic efficacy in modulating hepatic scar formation and resolution, offering new perspectives for chemokine-targeted antifibrotic therapy [34]. Importantly, the regulation of CCL5 is not unidirectional. Genetic deletion of CCL5 has been reported to induce compensatory upregulation of CCL2, which

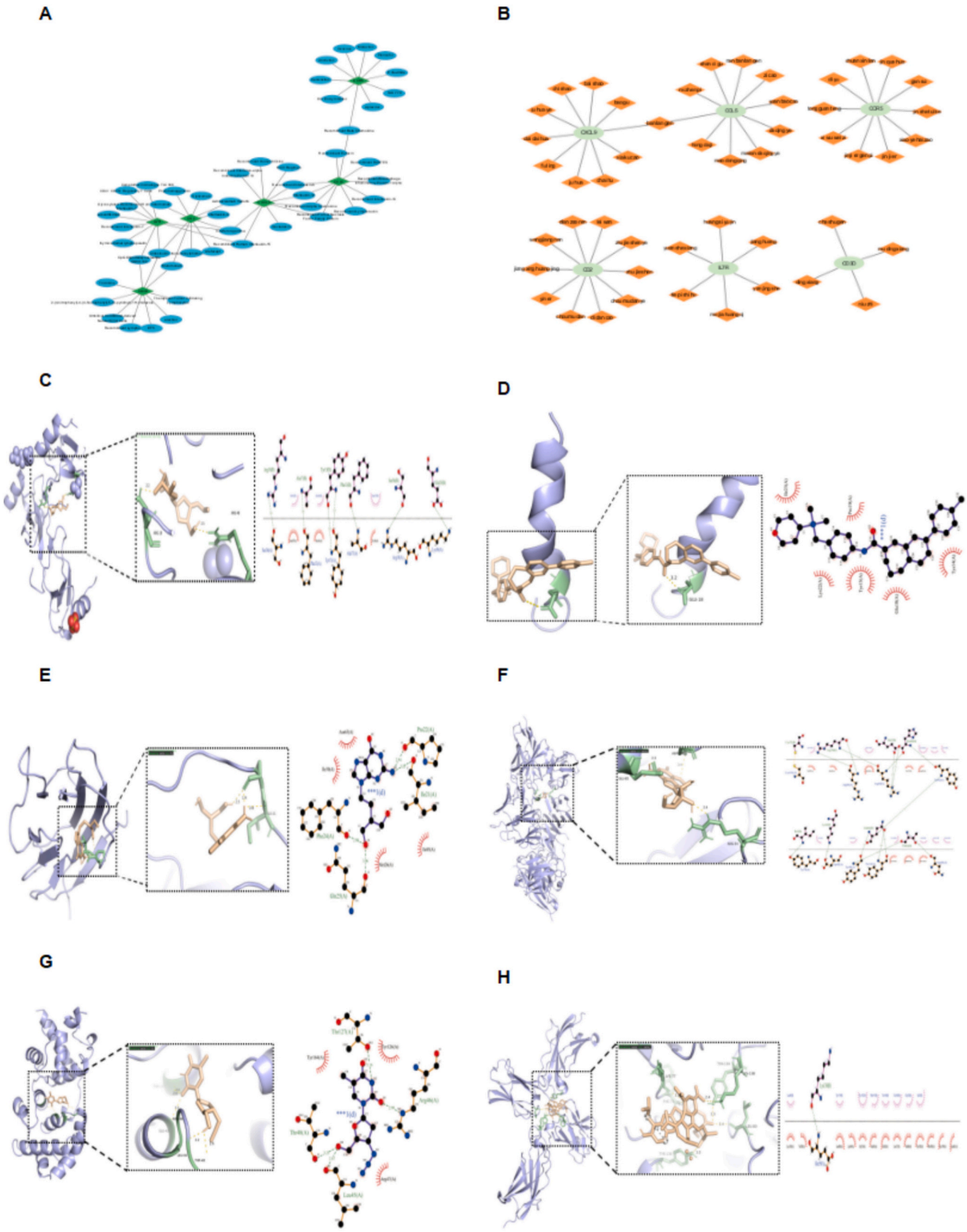

Fig. 10. Molecular docking of hub genes with candidate therapeutic compounds. Potential interactions between hub genes and therapeutic compounds were predicted using the Coremine database and visualized using Cytoscape. As shown in Figure A, drug–gene interaction networks illustrate the distribution of candidate small molecules targeting the identified hub genes. Figure B presents a similar network highlighting interactions between hub genes and compounds derived from traditional Chinese medicine. To validate the predicted interactions, molecular docking analysis was performed for each hub gene with its corresponding compound exhibiting the lowest binding energy. The resulting three-dimensional docking models (Figures C—H) demonstrate stable binding conformations characterized by spatial complementarity and hydrogen bonding interactions, providing structural evidence for the potential druggability of these targets.

activates RAAS-dependent inflammatory pathways, exacerbating renal injury and fibrosis [35]. This suggests a complex feedback relationship between CCL5 and other chemokines within the immune regulatory network and highlights the potential limitations of single-target interventions, emphasizing the need for combined modulation of multiple chemokine pathways. Our transcriptomic data, immune infiltration analysis, and regulatory network construction consistently support CCL5 as a central immunological chemokine in the early stages of renal fibrosis. We also identified several upstream regulators of CCL5, including miRNAs such as hsa-miR-619-5p, miR-7151-3p, and miR-5194, as well as transcription factors like RELA, SPI1, and RUNX1, further supporting its nodal role in the fibrotic regulatory landscape. Furthermore, molecular docking analysis revealed that the small-molecule compound TAK 779 could effectively target the CCL5–CCR5 axis, demonstrating favorable binding affinity and structural compatibility, thereby providing a theoretical basis and structural framework for clinical intervention strategies. In summary, CCL5 contributes to renal interstitial fibrosis through CCR5-mediated immune cell recruitment, activation of inflammatory pathways such as NF-κB and MAPK, and stimulation of fibroblast activity and collagen deposition—forming a key molecular axis from immune activation to fibrotic remodeling. As a central node coupling inflammation and fibrosis, CCL5 not only serves as a potential diagnostic biomarker for disease progression but also represents a promising therapeutic target for immune-modulatory anti-fibrotic interventions. Its multifaceted regulatory role merits further exploration in both experimental and clinical settings.

In addition to CD3D and CCL5, we also identified several other genes that may play pivotal roles in the pathogenesis of RIF. These genes appear to influence key biological processes such as immune cell activation, migration, and proliferation, thereby modulating immune responses and contributing to the progression of fibrosis through effects on immune cell infiltration, EMT, and ECM deposition. CD2, an important co-stimulatory molecule on the surface of T cells, facilitates interactions between T cells and antigen-presenting cells (APCs) by enhancing T cell activation and immunological synapse formation. This promotes immune cell infiltration and exacerbates inflammation [36]. In RIF, CD2-mediated T cell activation may intensify the activation and migration of renal interstitial cells, thereby accelerating fibrotic progression [37]. The expression of IL7R (interleukin-7 receptor) is also significantly altered in RIF. Through IL-7–mediated activation of IL7R signaling, T cell survival and proliferation are promoted, which can lead to hyperactivation of the immune system and disruption of immune homeostasis. This, in turn, exacerbates renal inflammation and fibrotic remodeling [38]. CXCL9, a pro-inflammatory chemokine, is markedly upregulated during inflammatory and fibrotic processes. It primarily exerts its effects by binding to its receptor CXCR3, thereby recruiting Th1 cells, natural killer (NK) cells, and other immune effectors to the site of injury, further amplifying renal immune damage and fibrosis [39]. Overexpression of CXCL9 has been closely associated with the progression of tubulointerstitial injury and is considered a potential early biomarker of fibrosis [36]. Moreover, CXCL9 may influence fibrosis through additional mechanisms. It can disrupt profibrotic cytokine pathways, such as by modulating TGF-β–GAG interactions, enhancing TGF-β signaling while preventing proteolytic degradation of the cytokine. Conversely, it may also inhibit leukocyte recruitment by competing with other chemokines for glycosaminoglycan (GAG) binding [40]. Together, these findings highlight the multifaceted roles of CD2, IL7R, and CXCL9 in modulating the immune microenvironment and contributing to the initiation and propagation of renal fibrosis. Their involvement in immune activation, cellular recruitment, and cytokine signaling underscores their potential as novel therapeutic targets in the treatment of RIF.

Through PPI network analysis and LASSO regression modeling, we identified a panel of hub genes with potential pathogenic relevance in fibrosis. Furthermore, we constructed corresponding upstream regulatory networks involving microRNAs and TFs, revealing a complex multilayered regulatory landscape potentially governing renal interstitial fibrosis. These regulatory axes not only deepen our understanding of the transcriptional and post-transcriptional mechanisms underlying key gene expression but also offer a theoretical foundation for targeted interventions via non-coding RNAs or TF modulators. Taken together, this study provides a genome-wide, systems-level characterization of the immunological underpinnings of renal interstitial fibrosis, identifying central molecular players and regulatory pathways that may serve as promising biomarkers for early diagnosis and targets for immune-based or personalized therapies. Moving forward, future investigations should focus on the functional validation of these hub molecules, leveraging advanced approaches such as single-cell transcriptomics, spatial multi-omics, and in vivo animal models to comprehensively evaluate their therapeutic potential and safety in clinical contexts.

5. Conclusion

In this study, we performed an integrated transcriptomic and bioinformatic analysis combined with immune infiltration assessment, functional enrichment profiling, PPI network construction, experimental validation, and molecular docking simulations to comprehensively delineate the immune-associated molecular landscape and therapeutic targets underlying RIF. We identified six key hub genes—most notably CD3D and CCL5—which exhibited marked upregulation in fibrotic tissues, strong correlations with immune cell infiltration, and robust diagnostic performance. Functional enrichment analyses (GO, KEGG, and GSEA) consistently highlighted their involvement in immune cell differentiation, migration, chemokine signaling, and interferon-mediated pathways, underscoring the immune-dominant nature of the fibrotic response. ssGSEA-based immune profiling and LASSO regression further demonstrated that CD3D and CCL5 play central roles in the recruitment and activation of pro-inflammatory immune subsets, including T cells, cytotoxic cells, and dendritic cells, suggesting they may amplify immune responses and exacerbate fibrotic progression through inflammation-driven mechanisms. These findings were experimentally validated in both murine UUO models and human CKD tissues, where CD3D and CCL5 were consistently upregulated at both mRNA and protein levels. Upstream regulatory analysis revealed a set of regulatory miRNAs (e.g., hsa-miR-370-3p, miR-7151-3p) and transcription factors (e.g., SPI1, RELA, RUNX1, FOXA1) that may modulate CD3D and CCL5 expression, providing mechanistic insight into their post-transcriptional control. Additionally, molecular docking simulations identified several promising small-molecule compounds—TAK 779, Triciribine, Interferon-gamma, and Recombinant Interleukin-6—all of which showed favorable binding affinities and spatial compatibility with hub gene targets, laying the groundwork for potential therapeutic development. Taken together, our study establishes a mechanistic and translational framework centered on the immune-regulatory CD3D–CCL5 axis in RIF, offering novel insights into its immunopathology and highlighting candidate biomarkers and druggable targets. This immunologically driven molecular framework provides a solid theoretical basis for improving diagnosis, prognostication, and immune-targeted therapies in renal fibrosis. Future studies should further explore this axis in vivo and develop targeted intervention strategies to advance precision medicine approaches for RIF.

Authors' contribution

SR initiated the idea, guided the article structure, and improved the final manuscript. MH reviewed the published studies and composed the draft of the manuscript. MH, AK, SG and HM provided critical feedback on drafts of the manuscript. All authors read and approved the final manuscript.

CRediT authorship contribution statement

Meng He: Writing – original draft, Visualization, Supervision, Resources, Project administration, Methodology, Investigation, Formal analysis, Data curation, Conceptualization. **Ayijiaken Kasimumali:** Resources, Project administration, Methodology, Funding acquisition, Formal analysis, Data curation. **Shunian Guo:** Validation, Supervision, Software, Resources, Project administration. **Hanyu Meng:** Supervision, Software, Resources, Project administration. **Shu Rong:** Writing – review & editing, Formal analysis, Data curation, Conceptualization.

Consent for publication

Not applicable.

Ethics approval and consent to participate

Not applicable.

Funding

This work was supported by the National Natural Science Foundation of China (No.82570867), Health Industry Clinical Research Special Project of Shanghai Municipal Health Commission (202340041) and Clinical Research Innovation Plan of Shanghai General Hospital (No. CTCCR-2021B09).

Declaration of competing interest

The authors declare that they have no known competing financial interests or personal relationships that could have appeared to influence the work reported in this paper.

Acknowledgements

Not applicable.

Data availability

Data will be made available on request.

References

[1] H. Jing, et al., Adiponectin in renal fibrosis, Aging (Albany NY) 12 (5) (2020) 4660–4672.
[2] C.J.L. Murray, The global burden of disease study at 30 years, Nat. Med. 28 (10) (2022) 2019–2026.
[3] R.G. Nelson, et al., Development of risk prediction equations for incident chronic kidney disease, Jama 322 (21) (2019) 2104–2114.
[4] J.Y. Duan, et al., Prevalence and risk factors of chronic kidney disease and diabetic kidney disease in a central Chinese urban population: a cross-sectional survey, BMC Nephrol. 21 (1) (2020) 115.
[5] A. Nogueira, M.J. Pires, P.A. Oliveira, Pathophysiological mechanisms of renal fibrosis: a review of animal models and therapeutic strategies, In Vivo 31 (1) (2017) 1–22.
[6] S. Klahr, J.J. Morrissey, The role of vasoactive compounds, growth factors and cytokines in the progression of renal disease, Kidney Int. Suppl. 75 (2000) S7–14.
[7] A. Kuma, M. Tamura, Y. Otsuji, Mechanism of and therapy for kidney fibrosis, J. UOEH 38 (1) (2016) 25–34.
[8] Y. Liu, New insights into epithelial-mesenchymal transition in kidney fibrosis, J. Am. Soc. Nephrol. 21 (2) (2010) 212–222.
[9] Y. Liu, Cellular and molecular mechanisms of renal fibrosis, Nat. Rev. Nephrol. 7 (12) (2011) 684–696.
[10] L.L. Falke, et al., Diverse origins of the myofibroblast—implications for kidney fibrosis, Nat. Rev. Nephrol. 11 (4) (2015) 233–244.
[11] R. Huang, P. Fu, L. Ma, Kidney fibrosis: from mechanisms to therapeutic medicines, Signal Transduct. Target. Ther. 8 (1) (2023) 129.
[12] W. Lv, et al., Inflammation and renal fibrosis: recent developments on key signaling molecules as potential therapeutic targets, Eur. J. Pharmacol. 820 (2018) 65–76.
[13] B.B. Lake, et al., An atlas of healthy and injured cell states and niches in the human kidney, Nature 619 (7970) (2023) 585–594.
[14] S.L. Lin, et al., Bone marrow Ly6Chigh monocytes are selectively recruited to injured kidney and differentiate into functionally distinct populations, J. Immunol. 183 (10) (2009) 6733–6743.
[15] F. Zhu, X. Bai, X. Chen, B lymphocytes in renal interstitial fibrosis, J Cell Commun Signal 11 (3) (2017) 213–218.
[16] K. Hochheiser, et al., Kidney dendritic cells become pathogenic during crescentic glomerulonephritis with proteinuria, J. Am. Soc. Nephrol. 22 (2) (2011) 306–316.
[17] R.D. Bülow, P. Boor, Extracellular matrix in kidney fibrosis: more than just a scaffold, J. Histochem. Cytochem. 67 (9) (2019) 643–661.
[18] P.M. Tang, D.J. Nikolic-Paterson, H.Y. Lan, Macrophages: versatile players in renal inflammation and fibrosis, Nat. Rev. Nephrol. 15 (3) (2019) 144–158.
[19] K. Yoshihara, et al., Inferring tumour purity and stromal and immune cell admixture from expression data, Nat. Commun. 4 (2013) 2612.
[20] G. Bindea, et al., Spatiotemporal dynamics of intratumoral immune cells reveal the immune landscape in human cancer, Immunity 39 (4) (2013) 782–795.
[21] G.E. McAuley, et al., Human T cell generation is restored in CD3δ severe combined immunodeficiency through adenine base editing, Cell 186 (7) (2023) 1398–1416.e23.
[22] Q. Deng, et al., The emerging epigenetic role of CD8+T cells in autoimmune diseases: a systematic review, Front. Immunol. 10 (2019) 856.
[23] J.I. Sanchez, et al., Cellular and molecular mechanisms of liver fibrosis in patients with NAFLD, Cancers (Basel) 15 (11) (2023).
[24] H.K. Dadi, A.J. Simon, C.M. Roifman, Effect of CD3delta deficiency on maturation of alpha/beta and gamma/delta T-cell lineages in severe combined immunodeficiency, N. Engl. J. Med. 349 (19) (2003) 1821–1828.
[25] Q. Yang, et al., CD3D and CD247 are the molecular targets of septic shock, Medicine (Baltimore) 102 (29) (2023) e34295.
[26] X. Lei, et al., CD3D silencing alleviates diabetic nephropathy via inhibition of JAK/STAT pathway, FASEB J. 38 (21) (2024) e70169.
[27] Q. Liu, et al., CCL5 suppresses klotho expression via p-STAT3/DNA Methyltransferase1-mediated promoter Hypermethylation, Front. Physiol. 13 (2022) 856088.
[28] Y. Qiu, et al., Myeloid-derived suppressor cells alleviate renal fibrosis progression via regulation of CCL5-CCR5 Axis, Front. Immunol. 12 (2021) 698894.
[29] X. Han, et al., Liquiritin protects against cardiac fibrosis after myocardial infarction by inhibiting CCL5 expression and the NF-κB signaling pathway, Drug Des. Devel. Ther. 16 (2022) 4111–4125.
[30] A.M. Krensky, Y.T. Ahn, Mechanisms of disease: regulation of RANTES (CCL5) in renal disease, Nat. Clin. Pract. Nephrol. 3 (3) (2007) 164–170.
[31] T. Wada, et al., Up-regulation of monocyte chemoattractant protein-1 in tubulointerstitial lesions of human diabetic nephropathy, Kidney Int. 58 (4) (2000) 1492–1499.
[32] E. Lefebvre, et al., Antifibrotic effects of the dual CCR2/CCR5 antagonist Cenicriviroc in animal models of liver and kidney fibrosis, PloS One 11 (6) (2016) e0158156.
[33] R. Sasaki, et al., Hepatitis C virus-induced CCL5 secretion from macrophages activates hepatic stellate cells, Hepatology 66 (3) (2017) 746–757.
[34] M.L. Berres, et al., Antagonism of the chemokine Ccl5 ameliorates experimental liver fibrosis in mice, J. Clin. Invest. 120 (11) (2010) 4129–4140.
[35] N.P. Rudemiller, S.D. Crowley, The role of chemokines in hypertension and consequent target organ damage, Pharmacol. Res. 119 (2017) 404–411.
[36] C. Binder, et al., CD2 Immunobiology, Front. Immunol. 11 (2020) 1090.
[37] A.S. Shaw, J.H. Miner, CD2-associated protein and the kidney, Curr. Opin. Nephrol. Hypertens. 10 (1) (2001) 19–22.
[38] J.T. Barata, S.K. Durum, B. Seddon, Flip the coin: IL-7 and IL-7R in health and disease, Nat. Immunol. 20 (12) (2019) 1584–1593.
[39] M. Metzemaekers, et al., Overview of the mechanisms that may contribute to the non-redundant activities of interferon-inducible CXC chemokine receptor 3 ligands, Front. Immunol. 8 (2017) 1970.
[40] S.H. Choi, et al., Dual-function synthetic peptide derived from BMP4 for highly efficient tumor targeting and antiangiogenesis, Int. J. Nanomedicine 11 (2016) 4643–4656.